IMAGING FLUID-RICH ZONES BY MAGNETOTELLURIC METHOD AT SOUTH MARMARA REGION

by

Özlem Cengiz

B.S., Geophysical Engineering, Süleyman Demirel University, 2008

Submitted to Kandilli Observatory and Earthquake
Research Institute in partial fulfillment of the
requirements for the degree of
Master of Science

Graduate Program in Geophysics
Boğaziçi University
2012

ACKNOWLEGEMENTS

I wish to express my thanks and gratitude to my supervisor Assist. Prof. Dr. Sabri Bülent Tank. His support and valuable advices throughout the thesis are gratefully appreciated. Sincere thanks also go to Elif Tolak Çiftçi, who was very helpful with ideas during my thesis. Many thanks to all those participated in the field work. Additionally, I would like to thank the instructors and M.Sc. fellows at the Boğaziçi University, Geophysics Department for their helps during the first stage of my academic life. Lastly, I am grateful for the continued support from my friends and family.

ABSTRACT

IMAGING FLUID-RICH ZONES BY MAGNETOTELLURIC METHOD AT SOUTH MARMARA REGION

Magnetotelluric data at sixteen sounding locations along two parallel profiles at south Marmara region were collected to improve the understanding of the crustal electrical conductivity structure. The PW (~40 km) and PE (~35 km) profiles yield data in the frequency range 320-0.0005 Hz. Remote reference technique (Gamble *et al.,* 1979) was used to enhance the data quality. The effects of near surface inhomogenities (galvanic distortions) were removed from the data utilizing Groom and Bailey (1989) decomposition. Following the decomposition, the geoelectric strikes of N102°E and N72°E were calculated for the PW and PE profiles, respectively. The data were rotated using these strike directions. Following this step, they were modeled in two dimensions using the inversion code developed by Ogawa and Uchida (Ogawa and Uchida, 1996), with error floors of 10 per cent for apparent resistivity and 2.86° for phase of both TE (transverse electric) and TM (transverse magnetic) modes. Resulting models suggest that the South Marmara fault possibly corresponds to a lateral resistive boundary between Manyas-Karacabey basin and Bandırma-Karadağ uplift on the PW and Uluabat uplift and Mudanya uplift on the PE profile. The features characterized in geoelectric models also correlate with known faults in the study area. While the conductive zones beneath the northern ends of the profiles at depths greater than 13 km are attributed to partially melting in the crust or the existence of deep crustal fluids below the impermeable layers, the highly resistive zones are associated with low fluid condition and high rigidity.

ÖZET

GÜNEY MARMARA BÖLGESİ' NDE MANYETOTELÜRİK YÖNTEM İLE SIVI İÇEREN ZONLARIN GÖRÜNTÜLENMESİ

Marmara Bölgesi'nin güney kısmında, kabuğun elektriksel iletkenlik özelliklerini incelemek amacıyla, birbirine paralel PW (~40 km) ve PE (~35 km) profilleri boyunca, 320-0.0005 Hz frekans aralığında, 16 farklı lokasyonda manyetotelürik veri toplanmıştır. Gürültülü manyetik alan ölçümlerine sahip istasyonlarda uzak referans (Remote Reference) (Gamble *ve diğ.*, 1979) yöntemi kullanılarak sinyal kalitesi arttırılmıştır. Yüzeye yakın üç boyutlu yapılardan kaynaklanan bozucu etkiler (galvanik bozulmalar) Groom ve Bailey (Groom ve Bailey, 1989) ayrıştırması kullanılarak empedans tensöründen atılmıştır. Sırasıyla PW ve PE için K102°D'lik ve K72°D'lik yerelektrik doğrultular hesaplanmıştır. Bu doğrultulara döndürülen MT verileri, görünür özdirenç için yüzde 10 ve faz için 2.86° hata ile hem TE (elektriksel olarak polarize olmuş) hem de TM (manyetik olarak polarize olmuş) biçim verileri kullanılarak, Ogawa ve Uchida (Ogawa ve Uchida, 1996) tarafından geliştirilen iki boyutlu ters çözüm programı ile modellenmiştir. Her iki profilden elde edilen yer elektrik modelleri Güney Marmara fayının PW profilinde Manyas-Karacabey havzası ile Bandırma-Karadağ yükselimi arasında, PE profilinde ise Uluabat yükselimi ile Mudanya yükselimi arasında bir sınır olduğunu göstermektedir. Elde edilen yer elektrik modeller bölgedeki bilinen faylar ile uyumludur. Kabukta bulunan iletken tabakalar kısmi ergime ya da kabuktaki geçirimsiz zonlarda hapsolmuş sıvılar ile ilişkilendirilirken, yüksek özdirence sahip tabakalar ise düşük sıvı muhtevası ve yüksek rijidite ile ilişkilendirilmiştir.

TABLE OF CONTENTS

LIST OF FIGURES

LIST OF TABLES

LIST OF SYMBOLS / ABBREVIATIONS

α	Rotation angle
A	Anisotropy tensor (in Groom and Bailey decomposition)
B	Magnetic induction
C	Roughening matrix
C	Frequency independent 2x2 real distortion tensor
D	Dielectric displacement
d	Predicted data
δ	MT skin depth
E	Electric field
e	Shear (in shear tensor)
ε	Dielectric permittivity
f	Frequency
F	Kernel function
F(m)	Model response
φ and β	Trade off parameters
Φ	Phase
Φ	Porosity
g	Site gain (in Groom and Bailey decomposition)
ρ	Electric charge density (in Gauss's Law)
ρ	Electrical resistivity
ρ_a	Apparent resistivity
H	Magnetic field
J	Electric current density
κ	Skew
m	Cementation or compaction exponent
m	Model parameter
μ	Magnetic permeability
R	Rotation matrix
S	Shear tensor (in Groom and Bailey decomposition)
Sw	Data misfit
s	Shear (in anisotropy tensor)

T	Period
t	Twist (in twist tensor)
T	Twist tensor (in Groom and Bailey decomposition)
T	Magnetic transfer function (tipper)
U	Misfit function
σ	Electrical conductivity
$\eth$	Standard deviation
W	Weighting matrix
w	Angular frequency
x,y,z	Cartesian coordinate axes, z positive downwards
Z	MT impedance tensor

1D	One-dimensional
2D	Two-dimensional
3D	Three-dimensional
PW	Western profile
PE	Eastern profile
BKU	Bandırma-Karadağ uplift
DF	Dereköy fault
DSFZ	Dead Sea Fault Zone
EAF	East Anatolian Fault
EAFZ	East Anatolian Fault Zone
EM	Electromagnetic
GB	Groom and Bailey
GPS	Global Positioning System
MKB	Manyas-Karacabey basin
MT	Magnetotellurics
MU	Mudanya uplift
NAF	North Anatolian Fault
NAFZ	North Anatolian Fault Zone
NEAFZ	Northeast Anatolian Fault Zone
r.m.s.	Root mean square

TE	Transverse electric mode (**E** polarization)
TM	Transverse magnetic mode (**B** polarization)
UB	Uluabat basin
UF	Uluabat fault
UU	Uludağ uplift
SMF	South Marmara fault

1. INTRODUCTION

The application of geophysical methods for near surface problems is a rapidly developing field. There are numerous geophysical methods based on different physical parameters that can be utilized in theoretical and practical studies. In this study, magnetotelluric (MT) method, a natural source electromagnetic (EM) technique, is used to elucidate electrical conductivity variations at a target area.

Natural source EM signals without a large transmitter and contact between source and receiver penetrate into the deeper parts of the Earth. They are also practically applicable to any location on the Earth since an additional deployment is not required to produce incident EM signals. The plane wave assumption is another advantage of natural source EM methods due to simpler mathematics for data analysis (Reynolds, 1997; Erkan, 2008).

The MT method was independently developed by Tikhonov (Tikhonov, 1950) and Cagniard (Cagniard, 1953). The fundamentals of method base on the principles of classical EM theory which was established years ago via the comprehensive works of Ampére, Faraday, Gauss and Maxwell. The behavior of EM fields at any frequency on the Earth's surface can be converted to apparent resistivity and phase with the help of Maxwell's equations; therefore, the information on electrical conductivity of subsurface at crustal or deeper scale can be obtained in light of the some analyzing and modeling tools (Simpson and Bahr, 2005).

The electrical conductivity (σ) (or its reciprocal (ρ), electrical resistivity) owing to the wide range of conductivity variations of crustal materials, gives independent information on the physical properties of the crust, which can be inaccessible by more conventional methods in some cases (Vozoff, 1991). Magnetotellurics is also the only geophysical technique capable of identifying the electrical conductivity structure from the

surface to the upper mantle (Bedrosian, 2007), which is why it has been primarily used to image electrical conductivity structure of the crust and mantle in many geophysical studies such as mineral surveying (Tuncer *et al.,* 2006), petroleum exploration (Constable *et al.,* 1998), active and fossil fault systems (Tank *et al.,* 2005; Ritter *et al.,* 2005), volcano studies (Aizawa *et al.,* 2005), crustal structures (Gürer, 1996; Bayrak and Nalbant, 2001), marine studies (Key and Constable., 1998), and hydrothermal systems (Nurhasan *et al.,* 2006).

The shallow and deep conductivity structure of tectonically active regions is widely imaged by magnetotellurics due to the fact that MT is one the most effective technique at detecting enhanced conductivity related to fluids such as groundwater, partial melting, aqueous fluids, brines and solids such as sulphides, magnetites and graphites in the crust (Jones, 1999; Jödicke, 1992; Ritter *et al.,* 2005; Bedrosian, 2007). The large scale conductivity within active tectonic regimes is associated with the existence of partial melt, aqueous fluids or a combination of partial melt and aqueous fluids (Li *et al.,* 2003). The conductivity of partial melts is strongly controlled by temperature, pressure, interconnectivity, the amount and concentration of water and compositional variations of rocks (*i.e.,* rock matrix) (Bedrosian, 2007).

Conductive zones which are generally called mechanically weak zones play a significant role before, during, and after earthquakes due to the fluid content (Zhao *et al.,* 1996). In this respect, the MT method has been applied to seek conductivity structure of the south Marmara region. We also aimed to link these geoelectric conditions to the geologic and tectonic states.

The thesis includes eight chapters. Chapter 1 introduces the study. The second chapter points out the method used in this study, the MT method. It highlights the source types, assumptions, some theoretical concepts such as apparent resistivity, phase, induction vectors, skin depth and the behavior of MT responses in the presence of layered half-spaces (1D, 2D and 3D). The dimensionality and distortions related to the effects of

surface heterogeneities on the MT responses is also the subject of this chapter. In the following chapter, Chapter 3, the tectonic and geological settings depending on previous studies at the target area are given. Chapter 4 briefly explains equipments, site locations, and data acquisition. The processing and modeling of observed data collected at the south Marmara region are discussed in Chapter 5. Finally, the discussions of the resulting 2D geoelectric models based on the sensitivity tests, and the conclusions are presented in the last two chapters of the thesis.

2. THEORY OF MAGNETOTELLURICS

2.1. Historical Development of the MT Method

The first papers related to the basis of one-dimensional (1D) MT analysis were propounded by Tikhonov (1950) and independently detailed by Cagniard (1953). Tikhonov suggested that at low frequencies, the derivative of horizontal magnetic field (**H**) is proportional to the ortohogonal component of the electric field (**E**). Cagniard, who is regarded as the pioneer to the method, developed the formulas concerning electric (**E)** and magnetic (**H)** fields on the surface of the layered medium with a plane wave source on his paper. The incident electromagnetic (EM) fields satisfying plane wave assumption at the surface was initially challenged and second-order corrections were suggested to Cagniard's formulation. However, the validity of Cagniard's assumptions was later proved. The horizontal magnetic field components need not be uniform, but can vary linearly over a layered Earth further demonstrated. The works of Tikhonov and Cagniard for 1D structure was later expanded by other geoscientists (Jiracek *et al.*, 1995).

2.2. The Source of the MT Signals

Natural electromagnetic fields in the MT method are used to image electrical properties of the Earth from surface to many tens of km, and these geoelectrical properties are linked to the subsurface conditions, physical state and tectonics deforming the crust (Jiracek *et al.*, 1995). The frequency range of natural EM signals extends from 10^{-4} to 10^{20} Hz (Jiracek *et al.*, 1995), but the frequency range of interest in MT method is from 10^{-4} to 10^{4} Hz. EM fields with frequencies lower than 1 Hz are produced by solar activity (Vozoff, 1991). EM signals at frequencies greater than 1 Hz (*i.e.*, periods shorter than 1 s) are constituted by worldwide lightning activity existing within the lower atmosphere (Vozoff, 1991). The so-called MT dead band around 1 Hz in which the natural EM fluctuations have a low intensity leads to the reduction in the quality of MT data (Simpson and Bahr, 2005).

2.3. Basic Theory of the MT Method

Electromagnetic waves propagate in space with mutually perpendicular and oscillating electric (**E**) and magnetic (**H**) field components are an indispensible part of MT method. An electromagnetic wave propagates in the positive x-direction and the electric (**E)** and magnetic (**H)** fields are perpendicular to each other and in phase, as demonstrated in Figure 2.1.

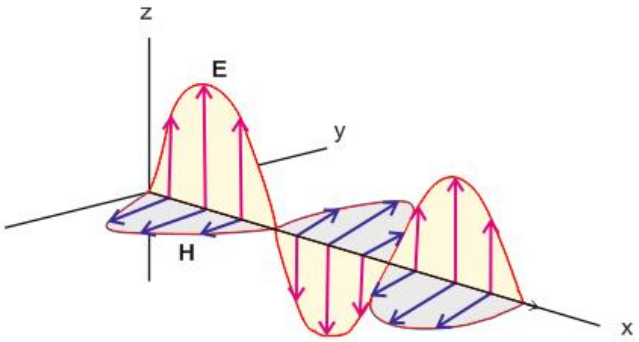

Figure 2.1. An electromagnetic wave with its two components, the electric (**E**) and magnetic (**H**) fields (redrawn from Ward and Hohmann, 1988)

As the EM energy reaches the surface of the Earth, reflection and refraction occur due to the fact that large conductivity contrast exists between the Earth (conductor) and air (insulator) (Vozoff, 1991). While the majority of incident energy is reflected from surface of the Earth (like in a boundary), a small portion of it is transmitted into the Earth and diffuse downward approximately 1-2 degree of vertical (Tikhonov, 1950; Cagniard, 1953; Vozoff, 1972, 1991; Jiracek, 1995). When the energy diffuses through ohmic losses in the Earth to the electrical conducting rocks, the primary time varying magnetic field induces a changing horizontal electric field at right angles, obeying Faraday's law, and the electric field drives the telluric currents (Vozoff, 1972, 1991; Kaufman and Keller, 1981). These

currents force the conductor to transmit a secondary time varying magnetic field through Ampére's law (Kaufman and Keller, 1981). The schematic illustration of induction of EM energy into the Earth is given in Figure 2.2.

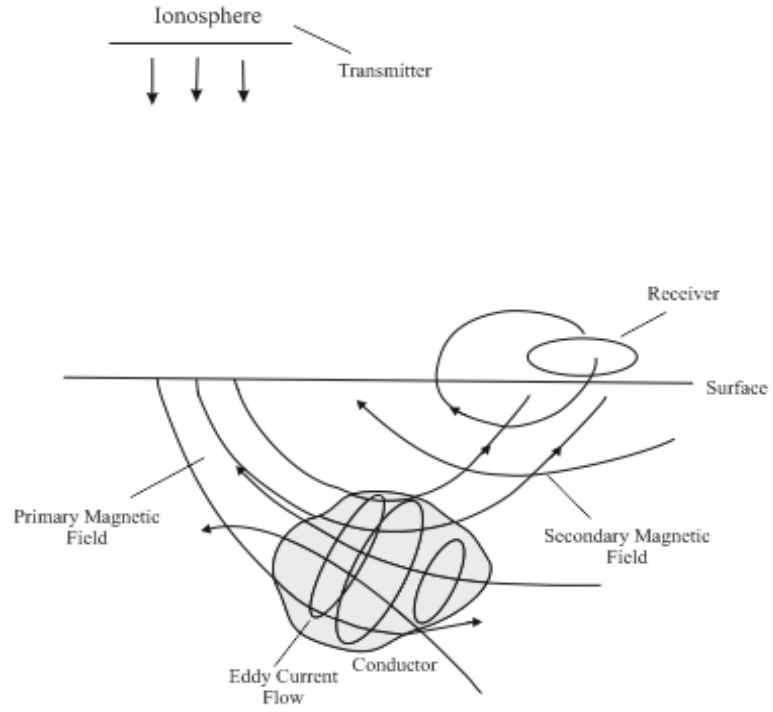

Figure 2.2. Electromagnetic induction theory (modified from Reynolds, 1997)

The EM field and also the electrical conductivity of rocks are responsible for the electrical currents that are induced in the ground. The charge transport within materials is described through the electrical conductivity (σ). Two types of conductivities, bulk and fluid conductivities, are mentioned because of this, the electrical properties of rocks dramatically depend on the pore geometry and fluid distribution in the rocks (Jones, 1999; Ritter *et al.*, 2005; Bedrosian, 2007). Bulk conductivity is significantly related to the volume of included fluid and its conductivity and the size and agreement of pores as well. Fluid conductivity is controlled by temperature, concentration of fluid in addition to the mobility and charge of ions (Ritter *et al.*, 2005). The empirical law of Archie (1942) explains the relation between fluid conductivity (σ_{fluid}) and bulk conductivity (σ_{rock}), which is given in its simplified form:

$$\frac{\sigma_{fluid}}{\sigma_{rock}} = \Phi^{-m} \tag{2.1}$$

where Φ is the porosity of the rock and m is the empirical coefficient called cementation or compaction exponent (Archie, 1942).

Electrical conductivity ranges over 10 orders of magnitude for rocks and rock-forming minerals of the Earth (Bedrosian, 2007). This wide range of electrical conductivity is strongly dependent on porosity, permeability, fluid saturation, salinity, solids such as graphites and sulphides, and properties such as temperature, viscosity and fluid types (Ritter *et al.,* 2005; Bedrosian, 2007). Resistivity values of several crustal rocks are given in Table 2.1.

Table 2.1. The range of electrical conductivity in earth materials (after Haak and Hutton, 1986)

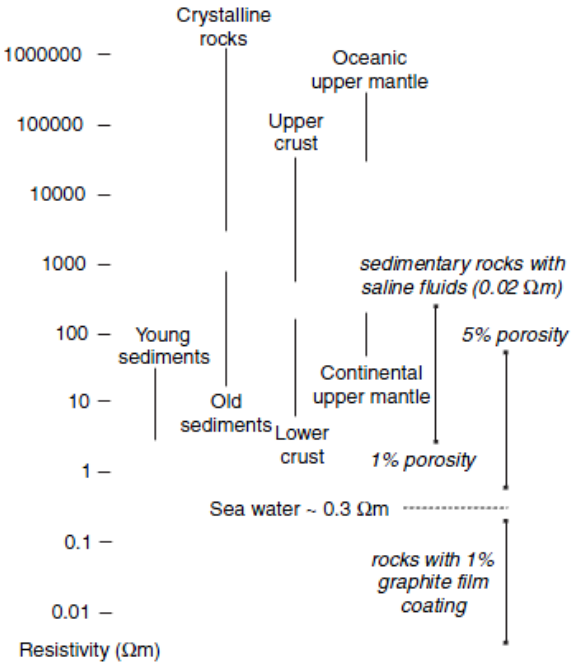

2.4. EM Diffusion in the Earth

The propagation of EM fields in the atmosphere and the Earth can be described by four equations known as Maxwell's equations. The four fundamental partial differential equations in time domain for a polarisable and magnetisable medium that contain no electric and magnetic sources may be expressed as (Ward and Hohhman, 1988):

$$\nabla \times \mathbf{E} = -\frac{\partial \mathbf{B}}{\partial t} \tag{2.2}$$

$$\nabla \times \mathbf{H} = \mathbf{J} + \frac{\partial \mathbf{D}}{\partial t} \tag{2.3}$$

$$\nabla . \mathbf{D} = \rho \tag{2.4}$$

$$\nabla . \mathbf{B} = 0 \tag{2.5}$$

where **E** is the electric field intensity (in V/m), **H** is the magnetic field intensity (in A/m), **B** is the magnetic induction (in Wb/m^2 or T), **J** is the electric current density (in A/m^2), **D** is the dielectric displacement (in C/m^2) and ρ is the electric charge density (in C/m^3).

The first of Maxwell's equations comes from Faraday's law, which physically means that the time varying magnetic fields induce electric fields. The second equation depends on Ampére's law modified by Maxwell by adding a new term called displacement currents (**D**=ε**E**). The other two equations are Gauss's law for the electric field (Equation 2.4) and for the magnetic field (Equation 2.5). While the generation of electric field by free charges is implied by the third equation of Maxwell, the last equation states that there are no free magnetic charges (magnetic monopoles).

The equations relating the electric and magnetic fields for linear isotropic materials are demonstrated as (Ward and Hohhman, 1988)

$$\mathbf{D} = \varepsilon \mathbf{E} \tag{2.6}$$

$$\mathbf{B} = \mu \mathbf{H} \tag{2.7}$$

$$\mathbf{J} = \sigma \mathbf{E} \tag{2.8}$$

where ε is the dielectric permittivity (in F/m), μ is the magnetic permeability (in H/m), and σ is the electrical conductivity (in S/m) of the medium. ε and σ are complex and depended on angular frequency ω, equal to $2\pi f$, whereas μ is a real quantity and assumed to be independent of frequency (Ward and Hohhman, 1988).

The electromagnetic diffusion equations in terms of time varying electric and magnetic fields are derived by utilizing Maxwell's equations and the Equations 2.6 through 2.8 for a homogenous linear isotropic medium.

Taking the curl of the Equations 2.2 and 2.3,

$$\nabla \times (\nabla \times \mathbf{E}) = -\nabla \times (\frac{\partial \mathbf{B}}{\partial t}) \tag{2.9}$$

$$\nabla \times (\nabla \times \mathbf{H}) = \nabla \times (\ \mathbf{J} + \frac{\partial \mathbf{D}}{\partial t}) \tag{2.10}$$

Substituting the Equations 2.6, 2.7 and 2.8 into the Equations 2.9 and 2.10,

$$\nabla \times (\nabla \times \mathbf{E}) = -\mu \frac{\partial}{\partial t} (\nabla \times \mathbf{H}) \tag{2.11}$$

$$\nabla \times (\nabla \times \mathbf{H}) = \sigma \nabla \times \mathbf{E} + \varepsilon \frac{\partial}{\partial t} (\nabla \times \mathbf{E}) \tag{2.12}$$

Rewriting the Equations 2.11 and 2.12 by coupling of the Equations 2.2 and 2.3,

$$\nabla \times (\nabla \times \mathbf{E}) = -\mu\varepsilon \frac{\partial^2 \mathbf{E}}{\partial t^2} - \mu\sigma \frac{\partial \mathbf{E}}{\partial t} \tag{2.13}$$

$$\nabla \times (\nabla \times \mathbf{H}) = -\mu\varepsilon \frac{\partial^2 \mathbf{H}}{\partial t^2} - \mu\sigma \frac{\partial \mathbf{H}}{\partial t} \tag{2.14}$$

The vector identities 2.15 and 2.16,

$$\nabla \times (\nabla \times \mathbf{E}) = \nabla . (\nabla . \mathbf{E}) - \nabla^2 \mathbf{E} \tag{2.15}$$

$$\nabla \times (\nabla \times \mathbf{H}) = \nabla . (\nabla . \mathbf{H}) - \nabla^2 \mathbf{H} \tag{2.16}$$

Assuming that $\nabla . \mathbf{E} = 0$ and $\nabla . \mathbf{H} = 0$ for homogenous regions and using the vector identities 2.15 and 2.16, then the Equations 2.13 and 2.14 can be shown that

$$\nabla^2 \mathbf{E} = \mu\sigma \frac{\partial \mathbf{E}}{\partial t} + \mu\varepsilon \frac{\partial^2 \mathbf{E}}{\partial t^2} \tag{2.17}$$

$$\nabla^2 \mathbf{H} = \mu\sigma \frac{\partial \mathbf{H}}{\partial t} + \mu\varepsilon \frac{\partial^2 \mathbf{H}}{\partial t^2} \tag{2.18}$$

where the electric and magnetic field diffusion equations in time domain are given in the Equations 2.17 and 2.18. While electromagnetic signals traveling by diffusion (conduction currents) are represented by the first term of the right hand side of Equation 2.18, the

second term represents wave propagation (displacement currents) which is significant for electromagnetic fields (Kaufman and Keller, 1981).

2.5. Assumptions in the MT Method

A set of simplifying assumptions in the EM induction theory are taken into consideration in defining apparent resistivity of sounding medium, which are given below:

- Maxwell's equations are obeyed in order to describe the behavior of the EM fields (Cagniard, 1953).

- The third equation of Maxwell, Gauss's law for the electric field (Equation 2.4), is the static-state case representation of law but the dynamic case (current flow) is the subject of the MT theory, which is why the equation becomes:

$$\nabla . \mathbf{E} = 0 \tag{2.19}$$

- The natural EM source fields generated by ionospheric and magnetospheric currents are used and these fields are assumed as plane-curves propagating vertically (normally) downwards into the Earth, (Vozoff, 1991).

- The Earth is assumed laterally uniform and all currents, the **E** and **H** fields are regarded as conservative and analytic away from the sources, which is an indication that the Earth acts as a good conductor to electromagnetic signals (Vozoff, 1972; Simpson and Bahr, 2005).

- The electrical permittivity ε and magnetic permeability μ for Earth materials change little from their free space values. The variations in ε and μ are thus assumed negligible compare to the variations in bulk conductivities and they are taken as constants in MT applications (Kaufman and Keller, 1981; Simpson and Bahr, 2005).

- The quasistatic approximation also paves the way to ignore the time varying displacement currents because of this the electrical conduction currents are much larger than the electrical displacement currents, which makes the EM induction clearly a diffusion process (Kaufman and Keller, 1981; Simpson and Bahr, 2005).

- Although the accumulation of free charges in the horizontally layered Earth are not expected, charges in the multi-dimensional (2D and 3D) Earth are assumed to accumulate at the boundary of conductive bodies, which is termed as static shift phenomenon (Simpson and Bahr, 2005).

2.6. The EM Impedance Tensor

In the MT method, the Earth is assumed as a linear and time invariant system. In this system, the Earth is termed as the transfer function and mathematically represented by the EM impedances. This linear relationship is expressed as follows (Vozoff, 1991)

$$\mathbf{E} = \mathbf{Z}\,\mathbf{H} \tag{2.20}$$

$$\begin{pmatrix} E_x \\ H_y \end{pmatrix} = \begin{pmatrix} Z_{xx} & Z_{xy} \\ Z_{yx} & Z_{yy} \end{pmatrix} \begin{pmatrix} H_x \\ H_y \end{pmatrix} \tag{2.21}$$

where each terms of the impedance tensor **Z** is frequency dependent, and it can be expressed as the amplitude (apparent resistivity) and phase at a particular frequency (Simpson and Bahr, 2005).

2.7. Apparent Resistivity, Phase and Skin Depth

The apparent resistivity and phase curves make it possible to present the result of EM field measurements in terms of frequency or period. Variations of apparent resistivity and phase values versus frequency are obtained from impedance tensor **Z**.

The apparent resistivity with respect to frequency in a non-uniform Earth is shown below (Bedrosian, 2007)

$$\rho_a = \frac{1}{\omega \mu} |\mathbf{Z}|^2 \tag{2.22}$$

where the Equation 2.22 is a mathematical representation of electrical resistivity (ρ) of sounding medium (in Ωm). While the equation in a homogenous Earth is equal to the exact value of electrical resistivity of medium, it is called apparent resistivity (ρ_a) in a non-uniform half-space (Jiracek *et al.,* 1995).

The changing electrical conductivity of sounding medium in a non-uniform Earth results in the phase of impedance tensor **Z**, which is phase differences between horizontal

components of the electric (E_x) and magnetic (H_y) fields, which can be expressed as below (Kaufman and Keller, 1981)

$$\Phi = arg\left[\frac{Im\,(Z_{xy})}{Re(Z_{xy})}\right] \tag{2.23}$$

where Φ is phase (in degree) and it is equal to 45° in homogenous Earth due to the fact that the conductivity of half-space does not change, and the component of the **E** and **H** fields are equal to each other. As the electrical conductivity of medium decreases with depth, the phase differences between E_x and H_y decreases and becomes less than 45°, and vice versa (Vozoff, 1972, 1991; Kaufman and Keller, 1981; Jiracek *et al.*, 1995).

The propagation of EM energy into the Earth is expressed by diffusion equations in terms of the **E** and **H** fields. The fact that the strength of these fields weaken exponentially (1/e≃0.37) with depth is known as a result of the solution of diffusion equations. The depth is dominantly controlled by conductivity of rocks and rock-forming minerals are termed the skin depth δ, and the formula of it is given as follows (Bedrosian, 2007)

$$\delta = \sqrt{\frac{2\rho}{\mu\omega}} \simeq 500\sqrt{\frac{\rho}{f}} \tag{2.24}$$

where δ , a specific distance (in m) called investigation or penetration depth, depends on the frequency (f) of incident EM fields.

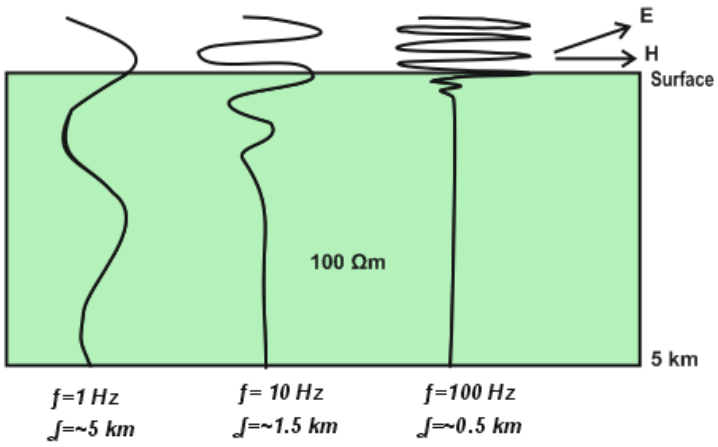

Figure 2.3. Physics of EM waves in a 100 Ωm half-space. f is frequency, δ is skin depth (modified from Unsworth, 2010)

2.8. One-Dimensional (1D) Earth

The electrical conductivity in the 1D Earth varies only with depth. The **E** and **H** fields are independent of the strike direction in such case. The vertical magnetic fields, in addition to the diagonal elements of impedance tensor vanish in the 1D Earth. Thus, the off-diagonal elements having equal magnitude, but opposite sign of the impedance tensor give the information about subsurface conductivity structure (Ritter *et al.*, 2005).

2.9. Two-Dimensional (2D) Earth

In the 2D Earth, electrical conductivity varying with depth and in one horizontal direction requires that the separation of Maxwell's equations into two different modes owing to the interaction between the components of EM fields and the strike. These modes are called transverse electric (TE, **E**-polarisation) and transverse magnetic (TM, **B**-polarisation) modes (Figure 2.4). While the electric currents are flowing along the strike in the TE mode, the flow in the TM mode is perpendicular to the strike (Simpson and Bahr, 2005). The modes can be described as:

$$\frac{\partial E_x}{\partial y} = -i\omega H_z \qquad \frac{\partial E_x}{\partial z} = -i\omega H_y \qquad \frac{\partial H_z}{\partial y} - \frac{\partial H_y}{\partial z} = \mu\varepsilon H_y \qquad \textbf{(TE mode)} \quad (2.25)$$

$$\frac{\partial H_x}{\partial y} = -i\omega E_z \qquad \frac{\partial H_x}{\partial z} = -i\omega E_y \qquad \frac{\partial E_z}{\partial y} - \frac{\partial E_y}{\partial z} = \mu\varepsilon H_x \qquad \textbf{(TM mode)} \quad (2.26)$$

where the length of strike is assumed much longer than the penetration depth and the variations of EM fields along the strike is also supposed zero (Simpson and Bahr, 2005).

The **E** and **H** fields interact mutually perpendicular to each other. The **E** parallel to strike (TE mode) induces **H** fields normal to the strike through Faraday's law. The **H** parallel to strike (TM mode) induces **E** fields normal to the strike, obeying Ampére's law. All components of EM fields, except the horizontal component of the **E** field, E_y, are continuous across the strike, and the current density in this direction is also continuous due to the conservation of charges (Vozoff, 1991; Simpson and Bahr, 2005).

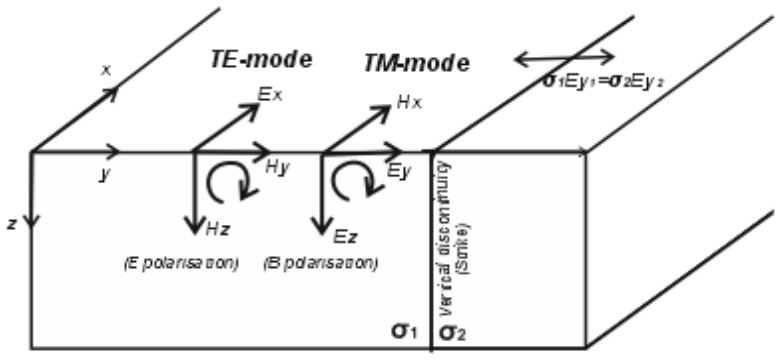

Figure 2.4. 2D resistivity model and the concept of TE and TM modes in magnetotellurics. E_y is discontinuous across the strike (modified from Simpson and Bahr, 2005 and Unsworth, 2010)

The ratios of the **E** and **H** field components, which are measured simultaneously during the MT survey, are then rotated in accordance with the geoelectric strike direction. In that way, it is computed that the different values of apparent resistivity ρ_{xy} and ρ_{yx} and phase Φ_{xy} and Φ_{yx} in terms of the different values of impedances Z_{xy} (TE mode) and Z_{yx} (TM mode). The TM mode is sensitive to lateral electrical conductivity variations in contrast to TE mode because of the discontinuity of E_y in TM mode. However, the TE mode provides the information concerning the vertical magnetic field transfer function that is the ratio of H_z and H_y and the other way of detecting the lateral conductivity changes (Simpson and Bahr, 2005).

The off-diagonal elements of impedance tensor in the perfect 2D Earth completely describe the impedance tensor shown below (Jiracek *et al.*, 1995)

$$\mathbf{Z}_{2D} = \begin{pmatrix} 0 & Z_{xy} \\ Z_{yx} & 0 \end{pmatrix} \tag{2.27}$$

where Z_{xy} and Z_{yx} are not equal to each other, in contrast to 1D case, and they represent the TE and TM mode impedances, successively.

In general, it is an unknown the direction of geoelectric strike prior to the MT survey, which is why, it is hardly possible to align the instruments in terms of the geoelectric strike direction in practice. In this respect, all elements of the impedance tensor are non-zero in real Earth. In such case, it is tried to either minimize the diagonal elements or maximize the off-diagonal elements to define the geoelectric strike direction. Swift (1967) analysis that is described in Section 2.12.2 is utilized to determine the strike direction (Vozoff, 1991).

The impedance tensor has 90° ambiguity in the strike orientation. Therefore, the rotation through 90° of impedance tensor in terms of geoelectric strike direction only changes the location of principal directions within the impedance tensor (Figure 2.5) (Swift, 1967; Lilley, 1998; Simpson and Bahr, 2005).

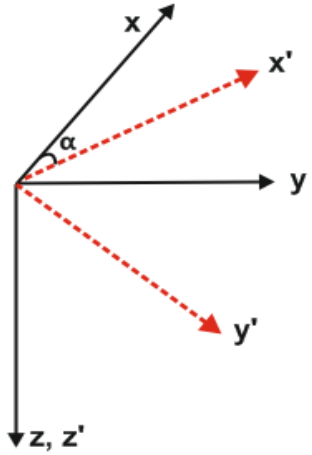

Figure 2.5. Orthogonal coordinate systems. The field coordinate axes (x, y, z) are rotated *a* degrees clockwise to the regional coordinate axes (x′, y′, z′) (modified from Swift, 1967)

The rotation can be shown that (Vozoff, 1991)

$$\mathbf{Z}_{2D} = \mathbf{R}\,\mathbf{Z}\,\mathbf{R}^{T} \tag{2.28}$$

where $\mathbf{R}$ and $\mathbf{R}^{\mathbf{T}}$ are the rotation and the transpose of the rotation matrix, respectively. $\mathbf{R}$ can be written as (Vozoff, 1991)

$$\mathbf{R} = \begin{pmatrix} cos\,\alpha & sin\,\alpha \\ -sin\,\alpha & cos\,\alpha \end{pmatrix} \tag{2.29}$$

where α or $\alpha \pm 90$ is the rotation angle and significant to determine the TE and TM modes in the 2D Earth.

2.10. Three-Dimensional (3D) Earth

The electrical conductivity in the 3D Earth varies with depth and in two horizontal directions. In the reality, measured MT responses are always 3D and the impedance tensor is fully occupied given the Equation 2.21. However, these 3D MT data are generally assumed as 2D with the help of dominant 2D characters of them. Thus, it is succeed much simpler data analysis than 3D case (Ledo, 2005; Ritter *et al.*, 2005).

2.11. Induction Vectors

The vertical magnetic field transfer functions characterizing a relationship between the vertical and horizontal magnetic field components are graphically presented by induction vectors (arrows). The vertical magnetic fields are assumed as zero in the absence of lateral conductivity variations. However, the existence of lateral conductivity gradients in the 2D Earth gives way to generation of the vertical magnetic fields in the TE mode through Faraday's law (Figure 2.6) (Jones, 1986; Vozoff, 1991; Jiracek 1995; Ritter *et al.*, 2005; Simpson and Bahr, 2005).

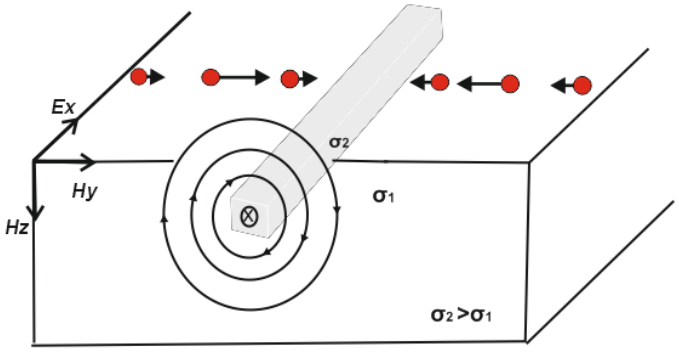

Figure 2.6. The concept of the vertical magnetic fields over a 2D Earth. Arrows denoting the real parts of induction vectors at each site (red circle) point toward the conductor (the Parkison (1962) convention) (modified from Unsworth, 2010)

The ratios of vertical to horizontal magnetic field components at any frequency can be written as (Vozoff, 1991)

$$H_z = \begin{pmatrix} T_x & T_y \end{pmatrix} \begin{pmatrix} H_x \\ H_y \end{pmatrix} \tag{2.30}$$

where T_x and T_y are complex magnetic field transfer functions variously called the tipper, induction or Parkinson vectors (Vozoff, 1991).

The vertical magnetic fields firstly mentioned by Parkinson (1962). They are used to obtain distortion free information on the geoelectric conditions of subsurface due to the independency of **E** components. The representation of vertical magnetic field transfer functions, induction vectors in the Parkinson convention point toward the regions of higher conductivity. These vectors align perpendicular to the geoelectric strike (Jones, 1986; Jiracek, 1995; Ritter *et al.*, 2005).

2.12. Distortions and Dimensionality of MT Data

2.12.1. Galvanic Distortion

The measured MT data in general involve the effects of near surface inhomogenities in addition to the time varying **E** and **H** fields as depending upon the subsurface structures. These small scale heterogeneities (surficial 3D bodies), which are conductive relative to the surrounding layered medium, perturb the measured **E** and **H** fields, and thus influences the impedance tensor through telluric (galvanic) and magnetic distortions (Vozoff, 1991; Jiracek, 1990, 1995; Ogawa, 2002).

Galvanic distortions, which are frequency independent non-inductive effects, occur when the depth of near surface 3D bodies are shallower than the penetration depth of EM waves. The distortion of the **E** through the charge accumulation at the boundary of the near surface 3D conductive bodies gives rise to the distortion of EM fields (Groom and Bailey, 1989; Jiracek, 1990; Simpson and Bahr, 2005). These distortions on EM fields can be mathematically described by real distortion tensors (Simpson and Bahr, 2005), as demonstrated below

$$\mathbf{C} = \begin{pmatrix} C_{11} & C_{12} \\ C_{21} & C_{22} \end{pmatrix} \tag{2.31}$$

where **C** is a frequency independent 2x2 real tensor.

Galvanic distortions can be categorized into two groups. These are distortions on amplitude (static shift) and phase (phase mixing) of the impedance tensor. Various methods are utilized to remove the effects of the near surface heterogeneities (local effects) from regional structure (Ogawa, 2002).

2.12.2. Swift Analysis

The determination of dimensionality and directionality of MT responses are crucial prior to modeling since the forward or inversion modeling is based on such properties of the MT responses. In order to define the geoelectric strike direction for observed MT data, several different methods (Swift, 1967; Bahr, 1988; Groom and Bailey, 1989; McNeice and Jones, 2001) have been suggested due to the fact that the diagonal elements of impedance tensor in real world are non-zero (Vozoff, 1972, 1991; Jiracek *et al.,* 1995).

Swift (1967) proposed to remove the deviations from a perfect 2D Earth by minimizing the sum of the diagonal elements of impedance tensor, and by maximizing the off-diagonal elements as well.

$$|Z_{xx}(\theta)|^2 + \left|Z_{yy}(\theta)\right|^2 \rightarrow \text{minimum} \tag{2.32}$$

$$\left|Z_{xy}(\theta)\right|^2 + \left|Z_{yx}(\theta)\right|^2 \rightarrow \text{maximum} \tag{2.33}$$

This yields the strike angle as,

$$4\theta_0 = \arctan \frac{(Z_{xx}-Z_{yy})(Z_{xy}+Z_{yx})^* + (Z_{xx}+Z_{yy})^*(Z_{xy}+Z_{yx})}{|Z_{xx}-Z_{yy}|^2 - |Z_{xy}+Z_{yx}|^2} \tag{2.34}$$

where * indicator of conjugate. Strike angle, Θ_0, which is also called Swift angle, is not true strike angle owing to the distortions on impedance tensor.

Since the strike orientation contains 90° ambiguity, either minimizing the diagonal or maximizing the off-diagonal elements of impedance tensor may not ensure a purely mathematical 2D Earth (Simpson and Bahr, 2005). Thus, Swift (1967) suggested a parameter, Swift skew κ, controls the accuracy of Swift analysis (empirical check).

$$\kappa = \frac{|Z_{xx}+Z_{yy}|}{|Z_{xy}-Z_{yx}|} \tag{2.35}$$

The Swift skew κ, which is commonly called skew or skewness, is a misfit measurement. The value of skewness parameter less than 0.3 is meaningful to calculate principle directions by Swift analysis (2D case), but it is meaningless for values greater than 0.6 (3D case) (Swift, 1967).

2.12.3. Groom and Bailey Decomposition

The aim of Groom and Bailey (1989) decomposition technique (GB decomposition) is to remove the effects of near surface inhomogenities (galvanic distortions) from measured impedance tensor (Groom and Bailey, 1989).

The measured impedance tensor $\mathbf{Z}_m$ in the Groom and Bailey scheme is decomposed as follows

$$\mathbf{Z}_m = \mathbf{RCZ}_{2\mathrm{D}}\mathbf{R}^{\mathrm{T}} \tag{2.36}$$

where $\mathbf{Z}_{2D}$ is the regional 2D impedance tensor which has only off-diagonal elements . $\mathbf{R}^{T}$ is transpose of rotation matrix **R**. **C** is a 2x2 distortion tensor and parameterized as below

$$\mathbf{C} = g\mathbf{TSA} \tag{2.37}$$

Substituting Equation 2.37 into Equation 2.36 yields

$$\mathbf{Z}_m = g\mathbf{RTSAZ}_{2D}\mathbf{R}^{T} \tag{2.38}$$

where g is a scalar termed site gain. T, S and A are named the twist, shear and anisotropy tensors, respectively and expressed as

$$\mathbf{T} = \frac{1}{\sqrt{1+t^2}}\begin{pmatrix} 1 & -t \\ t & 1 \end{pmatrix} \tag{2.39}$$

$$\mathbf{S} = \frac{1}{\sqrt{1+e^2}}\begin{pmatrix} 1 & e \\ e & 1 \end{pmatrix} \tag{2.40}$$

$$\mathbf{A} = \frac{1}{\sqrt{1+s^2}}\begin{pmatrix} 1+s & 0 \\ 0 & 1-s \end{pmatrix} \tag{2.41}$$

where t, e and s are real parameters called twist, shear and anisotropy, respectively.

Strike direction, twist and shear can be determined from GB decomposition, but site gain and anisotropy cannot be uniquely defined. The orthogonality of **E** and **H** fields are described by twist and shear whereas site gain and anisotropy are considered as an indicator of static shift that scales the apparent resistivity curve (McNeice and Jones, 2001; Ogawa, 2002).

The GB decomposition technique was later extended by McNeice and Jones (2001) for a set of sites over a given frequency band, which leads to the determination of optimal geoelectric strike direction for multiple sites and frequencies simultaneously with an assumed 2D regional resistivity structure distorted by local galvanic distortion. The use of multi-site-multi-frequency technique provides a stable estimate of the regional strike for entire data set over the whole frequency range (McNeice and Jones, 2001).

2.13. The Theory of MT data Modeling and Inversion

The final stage of MT data processing is to convert the frequency domain apparent resistivity and phase into true resistivity models. Inversion is applied to the apparent resistivity and phase curves in order to define the conductivity variations of the subsurface within an accepted threshold of tolerance (Simpson and Bahr, 2005).

It is aimed to predict the resistivity and phase values for the known Earth model in the forward modeling whereas the term of inversion is used to describe the process of estimating the model parameters on the basis of the model in order to compare the results of observed resistivity and phase values (Figure 2.7).

When **m**, **F** and **d** denote the model parameters, kernel function and predicted data, respectively, the forward modeling can be expressed as follows

$$\mathbf{d} = \mathbf{F}(\mathbf{m}) \tag{2.42}$$

where **m**=m_1, m_2, …, m_M and **d**=d_1, d_2, … ,d_N are vectors of M data and N measurements, successively.

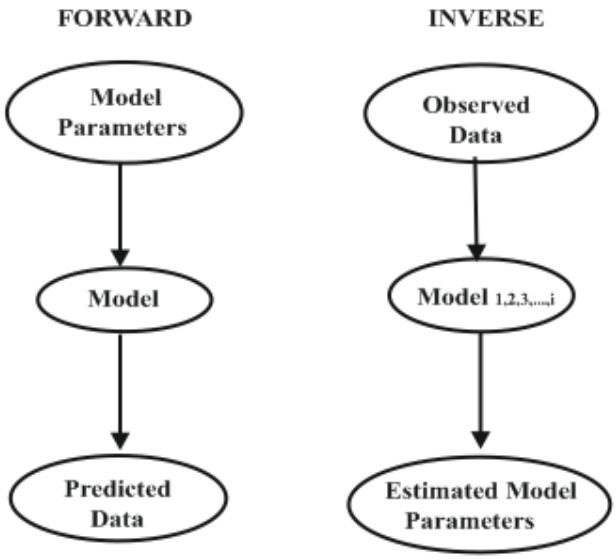

Figure 2.7. Flow diagram of forward and inverse modeling. The same data in the inverse modeling can generate many models due to the non-uniqueness (modified from Nowack, 2002)

In general, the inverse modeling performed to the field data in order to reveal the distribution of true physical properties from observed data can be shown as

$$\mathbf{F}(\mathbf{d}, \mathbf{m}) = \mathbf{d} - \mathbf{F}(\mathbf{m}) \tag{2.43}$$

where **F** is a non-linear forward function operating on the model **m** to obtain response (Uchida, 1993).

The MT inverse problem in practice is non-unique owing to data errors, spatially under-sampled data (M>N, ill-conditioned), a limited frequency band, model parameterization and physical assumptions, which is why, a regularization or a smoothness constraint is essential to impose the stability in the Equation 2.43 (Bedrosian, 2007).

In this study, the misfit **Sw** between observed resistivity and phase values is minimized by using two-dimensional inversion code of Ogawa and Uchida (1996). The inversion procedure in the code can be estimated with an L-2 norm measure,

$$\mathbf{Sw}(\mathbf{m}) = \|\mathbf{Wd} - \mathbf{WF}(\mathbf{m})\|^2 \tag{2.44}$$

where **m** contains the static shifts for each site and the logarithms of resistivity of each rectangular blocks within the model. **W** is the diagonal weighting matrix defined by data errors (Uchida, 1993):

$$w_{ii} = \frac{1}{\vartheta_i} \tag{2.45}$$

where ϑ_i is the standard deviation of i^{th} data error.

The smooth models in the code are achieved by minimization of misfit function **U** that is given below

$$\mathbf{U} = \|\mathbf{Wd} - \mathbf{WF}(\mathbf{m})\|^2 + \varphi^2\|\mathbf{Cm}\|^2 + \beta^2\mathbf{G} \tag{2.46}$$

where **C** is the roughening matrix (inverse of smooting) of the model parameters. φ and β are trade-off parameters. The larger values of φ and β lead to smoother models and the smaller static shift, respectively. The first term of right-hand side represents the misfit **S**, second term is called the roughness penalty of the model, and the final term is associated with the static shift which is taken into consideration as an inversion parameter (Ogawa and Uchida, 1996).

3. STUDY AREA, SOUTH MARMARA REGION

3.1. Tectonic and Geologic Settings of the Study Area

The tectonics of Turkey and its surrounding is quite complicated. The northward motions of the African and Arabian plates with respect to the relatively stable Eurasian plate squeezed the Anatolian block westward (Figure 3.1). Helenic Subduction Zone, continental collision in the eastern Anatolia and Caucasus are two forces that drive the tectonic evolution of eastern Mediterranean region. The combination of such mechanisms results in differences in the crustal structures. The northward motion of the Arabian plate relative to the Eurasia is giving rise to the crustal shortening and thickening in the eastern Anatolia whereas crust in the western Anatolia is much thinner due to the extensional regime controlled by the northward subduction of the African plate beneath western Turkey and Aegean region (Taymaz *et al.*, 2004).

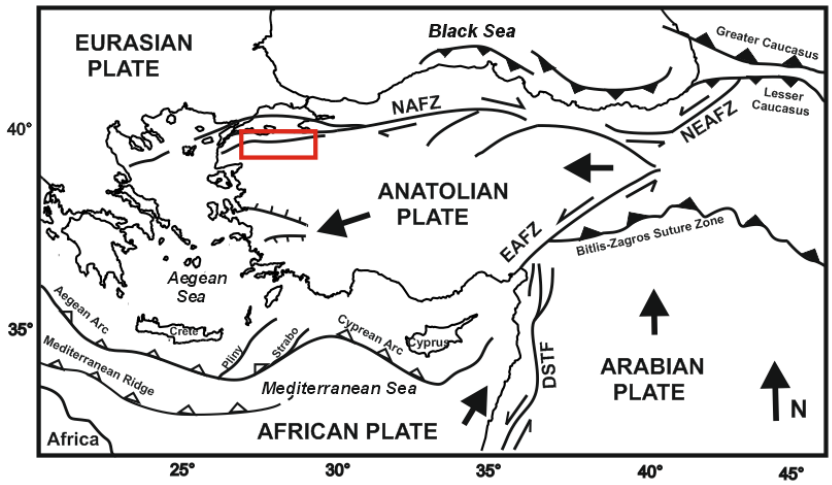

Figure 3.1. Simplified tectonic map of Turkey and surrounding (redrawn from Şengör *et al.*, 1985; Barka, 1992; Gürer and Bayrak, 2007). Red box indicates the area of this thesis. DSFZ – Dead Sea Fault Zone, EAFZ – East Anatolian Fault Zone, NAFZ – North Anatolian Fault Zone, NEAFZ – Northeast Anatolian Fault Zone

The Anatolian plate is bounded by two primary strike slip faults, the North Anatolian (NAF) and the East Anatolian Fault (EAF) (Figure 3.1). While the continental collision between Anatolian block and Arabian plate is responsible for the left lateral motion of the EAF, the NAF has a right lateral strike slip mechanism that accommodates the motion between Eurasian plate and Anatolian block. The NAF starts at Karlıova in the eastern Turkey and extends through the Marmara Sea to the Gulf of Saros in the northern Aegean is a ~ 1400 km long right lateral strike slip fault zone (Yılmaz *et al.,* 2006). A large part of its length is located some 100 km to the south of the Black Sea coast shows a simple character (Karabulut *et al.,* 2003). The NAF in the Marmara region, which is a transition zone between the right lateral strike slip regime of NAF and the extensional regime of the western Anatolia (Taymaz *et al.,* 2004), displays a complex character in account of stress regimes (Gürbüz *et al.,* 2000), and experienced several damaging earthquakes such as İzmit earthquake (M_W=7.4, 1999) and Düzce earthquake (M_W=7.2, 1999).

The result of the extension over the strike slip regime in the Marmara region gives rise to the division of NAF into three branches. These are northern, middle and southern branches (Gürer *et al.,* 2003). The northern branch extends through İzmit and Karamürsel basins, and enters into the northern margin of the Marmara Sea. The middle branch passes through Geyve basin, continues between Armutlu and Kapıdağ peninsulas, then crosses Biga peninsula, and enters the Aegean Sea at Ezine. The southern branch extends through Bursa and Manyas-Karacabey basins, traverses the Biga peninsula, passing by Gönen and Pazarköy, and enters the Aegean Sea at Edremit Bay (Gürbüz *et al.,* 2000). This study was carried out in the area involved by middle and southern branches.

The seismic activity in south Marmara region is controlled by the middle and southern strands of NAF (Gürer *et al.,* 2003). Morphological structure in the study area is also dominated by active faulting. Most of the faults in this region are right lateral strike slip but some of them are normal faults. Uluabat and Manyas-Mustafakemalpaşa faults are right lateral strike slip faults with normal components, Yenice-Gönen and Karacabey faults are right lateral strike slip faults. The south Marmara, Dereköy and Bursa faults are normal

faults (Selim and Tüysüz, 2005; Selim *et al.,* 2006). The seismicity map of the study area is shown in Figure (3.2).

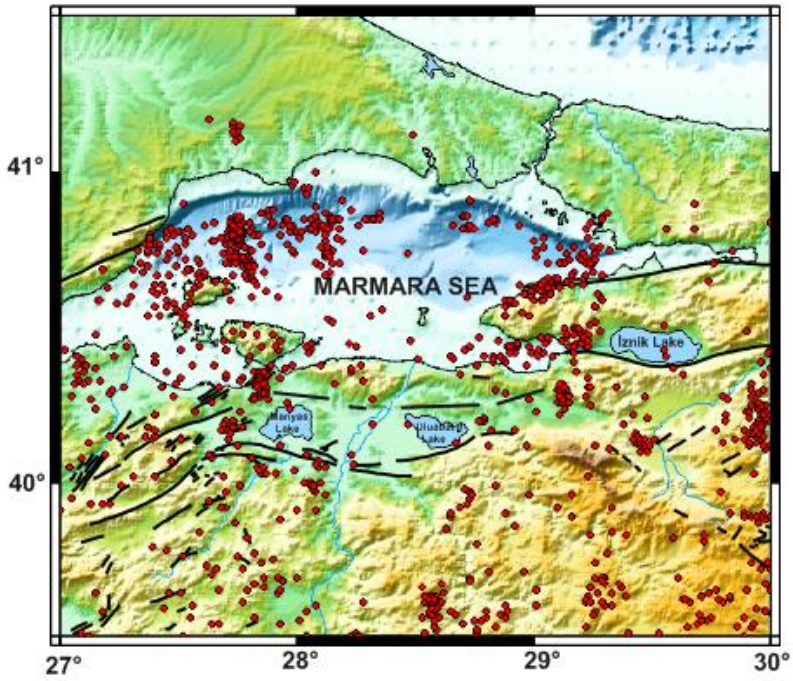

Figure 3.2. Seismicity map of the study area. Black lines show active faults at the region. Red circles are the earthquakes (observed for one year (2011), B.U., Kandilli Observatory and Earthquake Research Institute)

MT lines were located at the area between the middle and southern branches of NAF. The PW profile crosses the Bandırma-Karadağ uplift and Manyas-Karacabey basin (Figure 3.3). While Bandırma-Karadağ uplift formed by normal faulting, Manyas-Karacabey basin is a pull-apart basin and formed by NE-SW trending extensional stress regime. The PE profile crosses the Mudanya uplift, Uluabat basin and Uludağ uplift (Figure 3.3). Mudanya and Uludağ uplifts formed by normal faulting (Selim *et al.*, 2006). On the other hand, Uluabat basin is a pull-apart basin and formed by NE-SW trending extensional stress regime (Selim and Tüysüz, 2005).

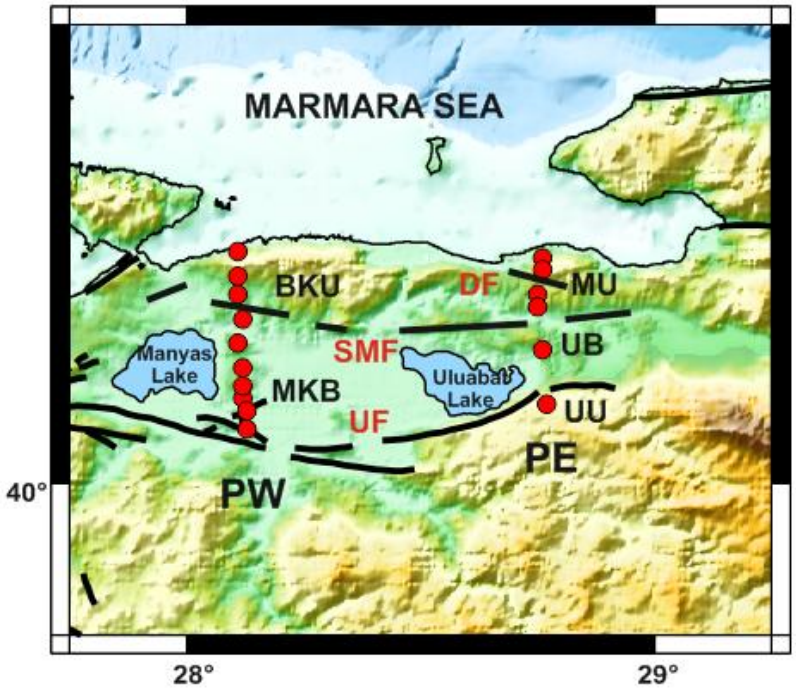

Figure 3.3. Locations of MT stations (red dots) at survey area. PW: West profile, PE: East profile, BKU: Bandırma-Karadağ uplift, MKB: Manyas-Karacabey basin, MU: Mudanya uplift, UB: Uluabat basin, UU: Uludağ uplift, SMF: DF: Dereköy fault, SMF: South Marmara fault, UF: Uluabat fault

3.2. Previous Studies

After the mainshock of İzmit earthquake, scientists have undertaken various kinds of observations in the Marmara region in order to increase understanding of crustal properties of North Anatolian Fault Zone (NAFZ) (Le Pichon, 2003; Karabulut *et al.*, 2003; Tank *et al.*, 2005; Gürbüz *et al.*, 2000). Most of these studies are related to the east Marmara region since the destructive earthquakes occurred there.

Ulugergerli *et al.*, (2007) investigated the shallow and deep conductivity structure of western Anatolia along a 290 km long profile by MT measurements. The geoelectric models, constituted from 2D joint inversion of TE and TM mode data, then verified by

utilizing gravity and magnetic data. In this study, the conductive (<10 Ωm) and resistive zones beneath the central and southern branches of NAF and western Anatolia were imaged. The shallow and deep conductive zones in the geoelectric models were associated with sedimentary basins and hot areas, respectively, whereas the highly resistive regions were interpreted as major structures.

Several GPS studies in the study area suggest the existence of an independent microplate which is bounded by the northern and southern branches of NAF (Meade *et al.*, 2002; Le Pichon *et al.,* 2003; Flerit *et al.,* 2003; Nyst and Thatcher, 2004). In these studies, the southern part of Marmara region is described as the South Marmara Block by GPS velocity vectors.

Hisarlı (1995), by analyzing aeromagnetic maps estimated Curie point depth of between 8 and 12 km for Edremit, Susurluk and Balıkesir regions. The Earth's magnetic field vectors in the area demonstrate uniform variations. When the map of Curie depth points was compared with the gravity, magnetic and geological map of the area, it was seen consistency between them. Aydın *et al.,* (2005) have prepared a Curie point isotherm map of the whole of Turkey from the aeromagnetic data. In this study, the Curie point depths are estimated to be about 15 km along the southern branch of the NAF and 10-12 km for Bursa region. Dolmaz *et al.,* (2005) by analyzing aeromagnetic data estimated Curie point depth of between 8.2 and 19.9 km in western Anatolia. The shallow Curie depth of the Marmara Sea is also determined by utilizing aeromagnetic data in the study (Ateş *et al.,* 2003).

The heat flow map of Tezcan (1979), İlkışık (1995) and Hisarlı (1995) show the thermal state of the crust in western Anatolia. In these studies, Tezcan (1979) was suggested the heat flow value of 90-100 mW/m°C in southern part of Marmara region. İlkışık (1995) and Hisarlı (1995) were also estimated the value of heat flow as 66-110 mW/m°C and 95-134 mW/m°C in the region, respectively.

Gravity modeling in the southern Marmara Sea and its surrounding were constructed in order to describe the distribution of the gravity field in the region (Adatepe *et al.,* 2002). Low gravity values for the Miocene-Pliocene sedimentary sequences and high values for uplifted areas were concluded in the study. 2D gravity and magnetic models in the Marmara Sea and its surrounding were prepared to provide further detailed information on the deep structure of the region. The gravity model displays that the existence of horst-like structures (Ateş *et al.,* 2003, 2008).

4. FIELD DATA ACQUISITION

4.1. Magnetotelluric Data Acquisition

The wide band MT data were collected in the area involved by the middle and southern branches of the NAF in south Marmara region. The measurements at 10 sites on the PW profile and 6 sites on the PE profile were carried out during the survey (Figure 4.1). High quality MT responses in the target area were obtained for developing the electrical resistivity structure of the subsurface.

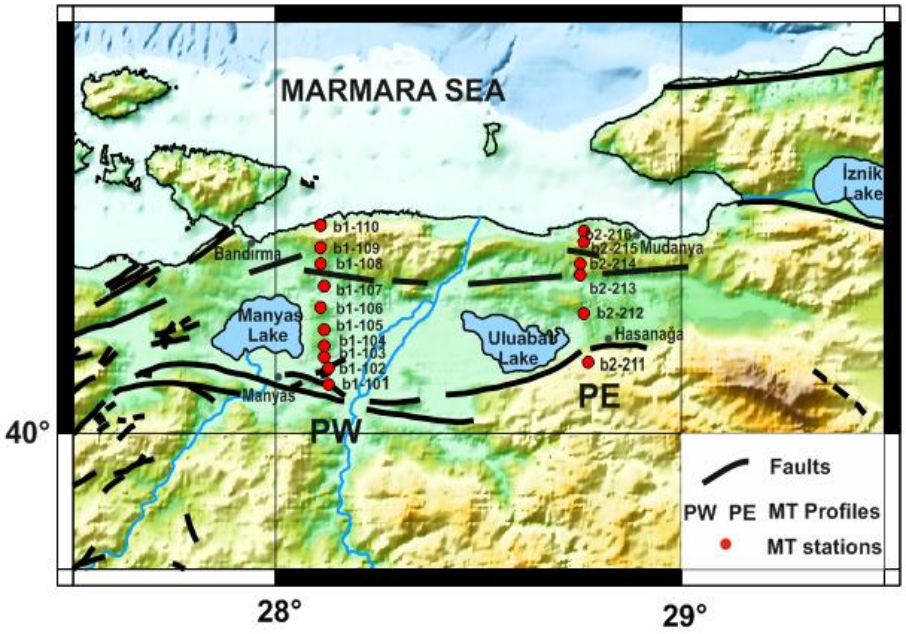

Figure 4.1. The map showing the location of profiles with MT stations

The PW profile extends from Bandırma to Manyas. The site separation at PW profile ranges from 1.7 km to 6 km (Figure 4.1). This profile is approximately 40 km long. The PE profile is deployed almost 54 km to the east of the PW profile and extends from Mudanya to Hasanağa (Figure 4.1). The site separation on this profile ranges between 2.9 and 10.8. The length of this profile is almost 35 km long. Therefore, in total 16 wide band

MT stations along two parallel profiles were used (Figure 4.2). The time varying EM fields at each site were recorded 1 day and remote reference technique (Gamble *et al.*, 1979) was performed at the stations containing noisy magnetic field.

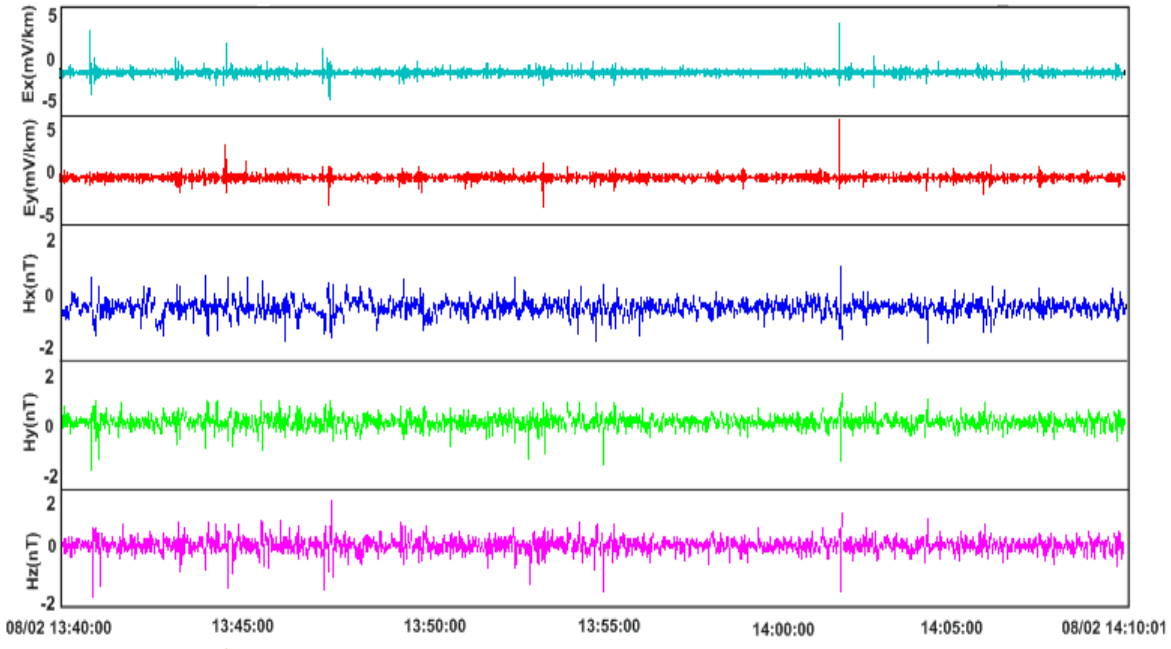

Figure 4.2. A sample time series segment of 30 min for the station b1-107

4.2. Magnetotelluric Instrumentation

MT data at 16 sites were recorded using five Phoenix MTU 5A systems. These instruments record **E** and **H** fields at the surface of the Earth. The instruments are synchronized by time signals from GPS satellites. The frequency range of these instruments extends from 320 Hz to 0.0005 Hz. The geomagnetic north was taken as the reference direction when setting the sites. For **E** measurements, five non-polarizable Pb-$PbCI_2$ electrodes were utilized in order to measure the time varying potential differences between two electrodes. The east-west and north-south oriented dipoles measured two horizontal components of **E**. The fifth one, grounding electrode was located at the center of

the site. The contact resistance between the electrodes and the soil was maintained by burying the electrodes in salty mud. For **H** measurements, three induction coils were used to measure three perpendicular components of **H** (Figure 4.3).

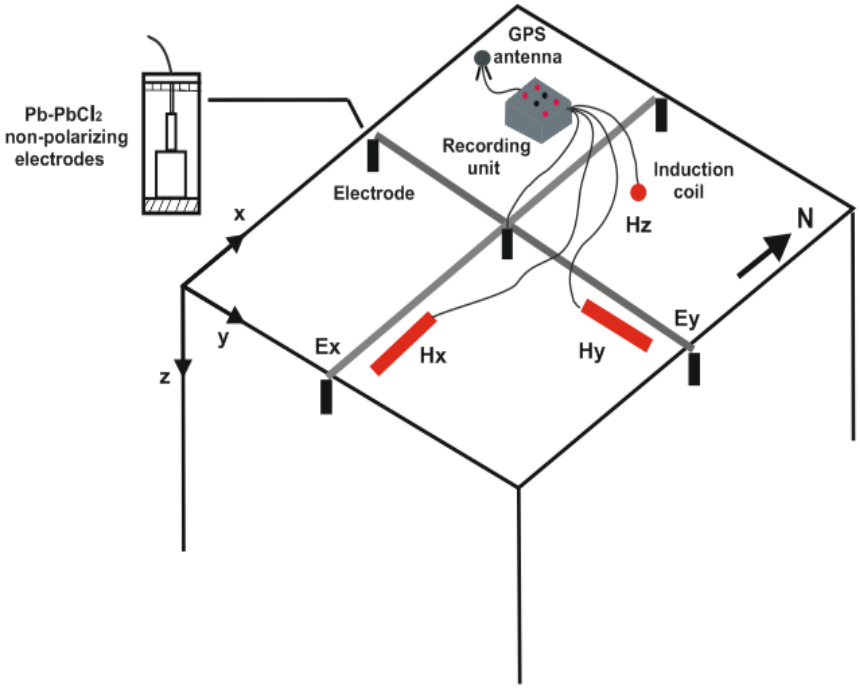

Figure 4.3. Sketch of magnetotelluric site layout with EM fields

5. DATA PROCESSING

The processing steps such as converting the time series data to frequency domain, remote reference, decomposition of impedance tensor and modeling of observed MT data are laid in this chapter. The entire process of observed data in this thesis was achieved in light of the information given in the previous chapters. Processing steps used for the MT data sets are given in the Figure 5.1.

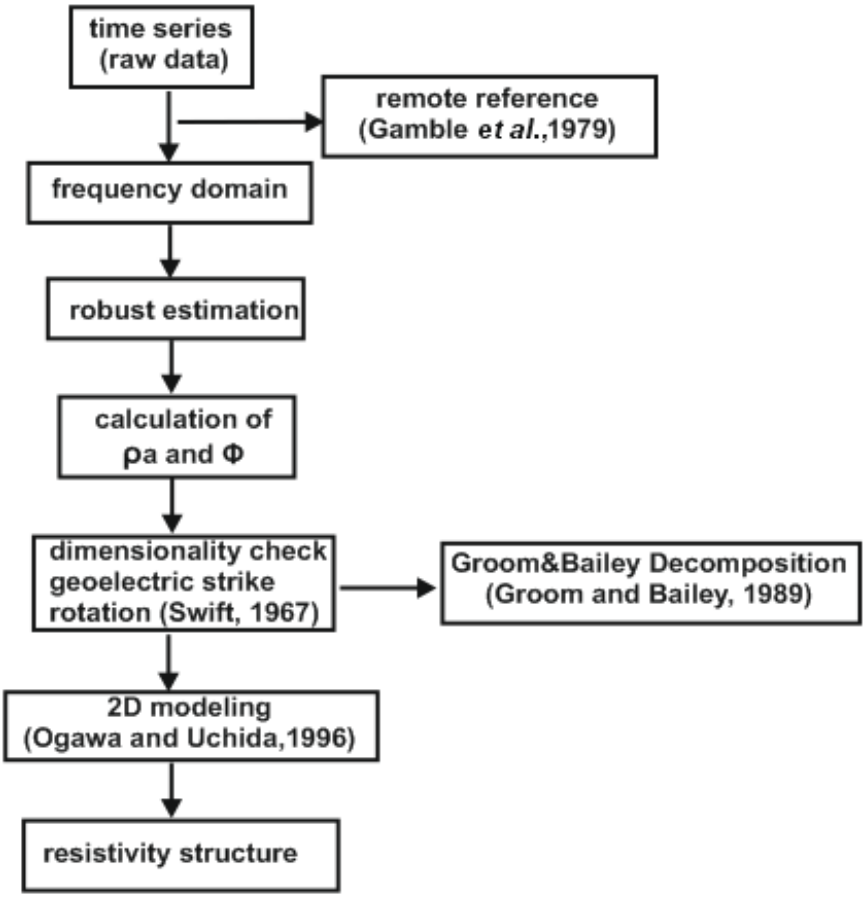

Figure 5.1. Flow diagram of processing steps used for the south Marmara data

When transforming the time domain data to frequency domain, Fast Fourier Transform (FFT) was utilized. The remote reference technique (Gamble *et al.*, 1979) was used to remove noisy data by means of a reference station. Then, the impedances were calculated, and the apparent resistivity and phase were obtained.

5.1. Tensor Decomposition

The multi-site-multi-frequency decomposition technique of McNeice and Jones (2001) in the MT data processing was used to decompose the south Marmara data sets. This technique allows the statistical fit of the single-site-single-frequency calculations to multi-site-multi-frequency calculations.

The shear angle, twist angle and r.m.s misfit values derived from the Groom and Bailey (1989) decomposition for the whole frequency band of each site are displayed in Figure 5.2. These values of twist and shear angles indicate minor galvanic distortion. The small values of r.m.s. misfit are also shown in Figure 5.2 displaying the accuracy of the decomposition.

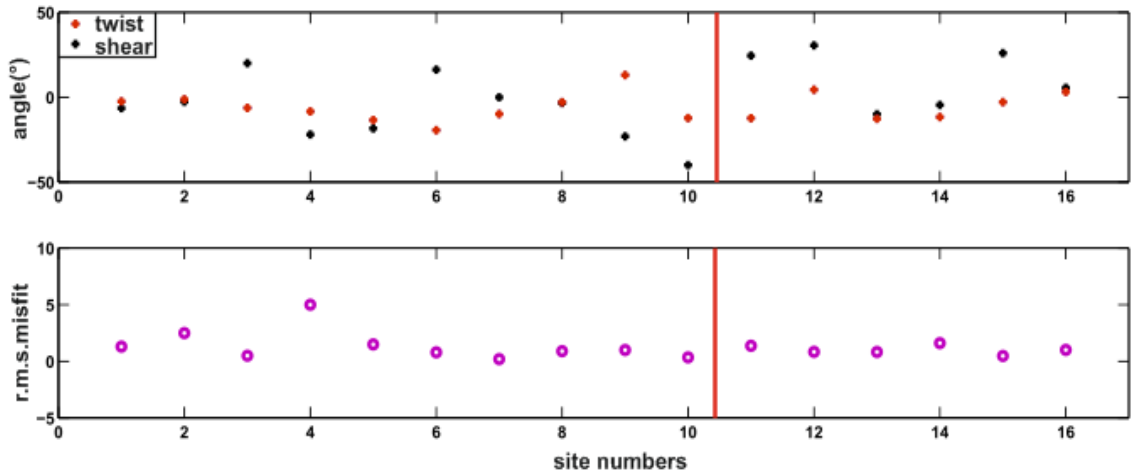

Figure 5.2. Shear angle, twist angle and r.m.s misfit variations for the whole frequency band of each site. Red line is the boundary between PW and PE profiles

The elimination of galvanic effects from the measured impedance tensor ensured the stable estimate of the regional strike for entire data set over a frequency range. The geoelectric strike variations along two parallel profiles were determined at each site, in addition to all sites (Figure 5.3). In this way, frequency-site dependent and frequency-site independent geoelectric strike variations were obtained for both profiles (Figures 5.3 and 5.4).

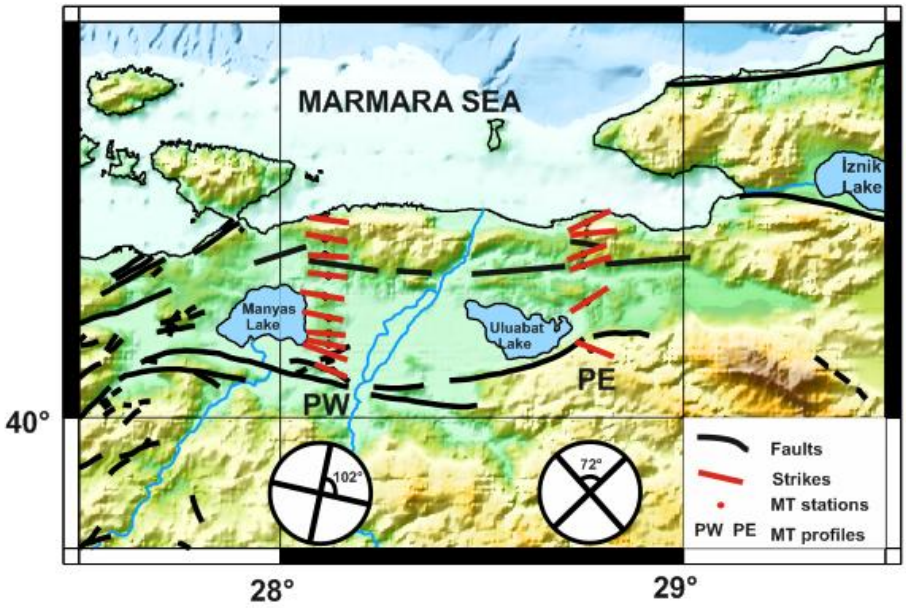

Figure 5.3. Strikes at each station for the whole frequency range from the tensor decomposition

In south Marmara region, the geoelectric strike of N102°E and N72°E were calculated for PW and PE profiles, respectively (Figure 5.3), by using the multi-site-multi-frequency tensor decomposition analysis for all sites over the whole frequency band. These values of geoelectric strikes are well consistent with the regional geological strike. Strike directions shown in Figure 5.3 vary between N117°E and N98°E in PW and N63°E and N82°E in PE profiles.

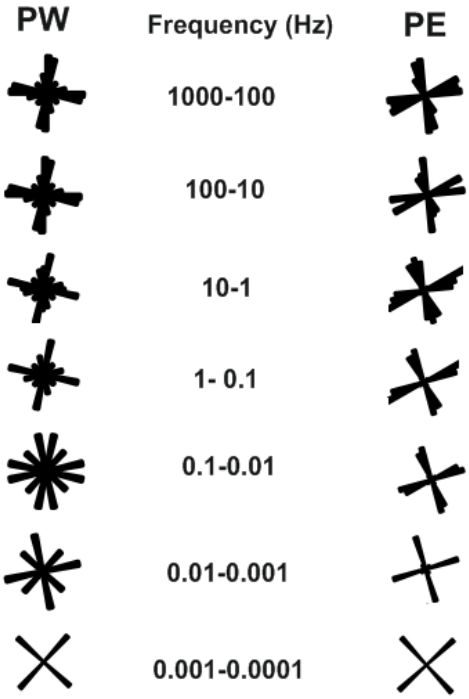

Figure 5.4. Strikes of PW and PE for separate range

Rose diagrams in Figure 5.4 show the geoelectrical strike from the tensor decomposition for both profiles in the frequency range from 1000 to 0.0001 Hz. The geoelectric strike values for the undistorted MT data demonstrate the similar strike directions at high (shallow structure) and low frequencies (deeper structure) (Figure 5.4).

The small values of skew (<0.3) demonstrated in Figure 5.5 are indicating the 2D resistivity structure of the study area. The larger values of skew (>0.3) at high frequencies represent the existence of small scale heterogeneities (surficial 3D bodies) at shallow depths (Figure 5.5). Therefore, we can say that the south Marmara data set is dominantly 2D and appropriate to 2D interpretation.

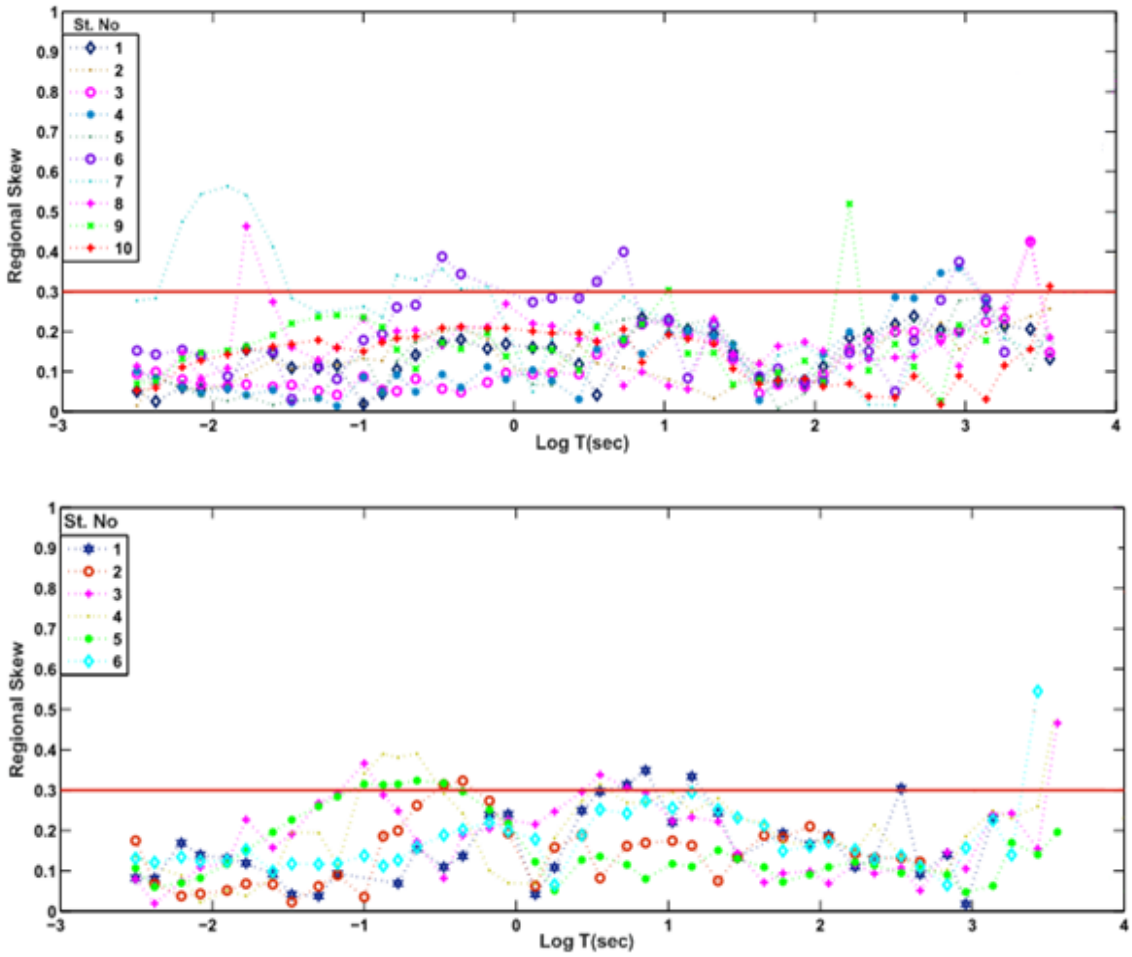

Figure 5.5. Swift's skew value for all sites on the PW (upper) and PE (bottom) profiles. Red line is the boundary of 2D

The electrical conductivity contrast between land and seawater leads to spread out electric currents along the coasts (Park *et al.*, 1991), which is known as coast effect. The real part of induction vectors in the Parkinson convention (1962) plotted for three different frequencies (120, 0.1 and 0.01 Hz) to characterize the effect of the southern coast of the Marmara Sea (Figure 5.6). These vectors point toward the regions of high conductivity and the lengths of them describe the magnitudes of conductors. At 120 Hz, vectors are scattered owing to the effects of surface inhomogenities. The direction and increasing length of the vectors towards the shore of the Marmara Sea at 0.01 Hz completely characterize the coast effects (Figure 5.6).

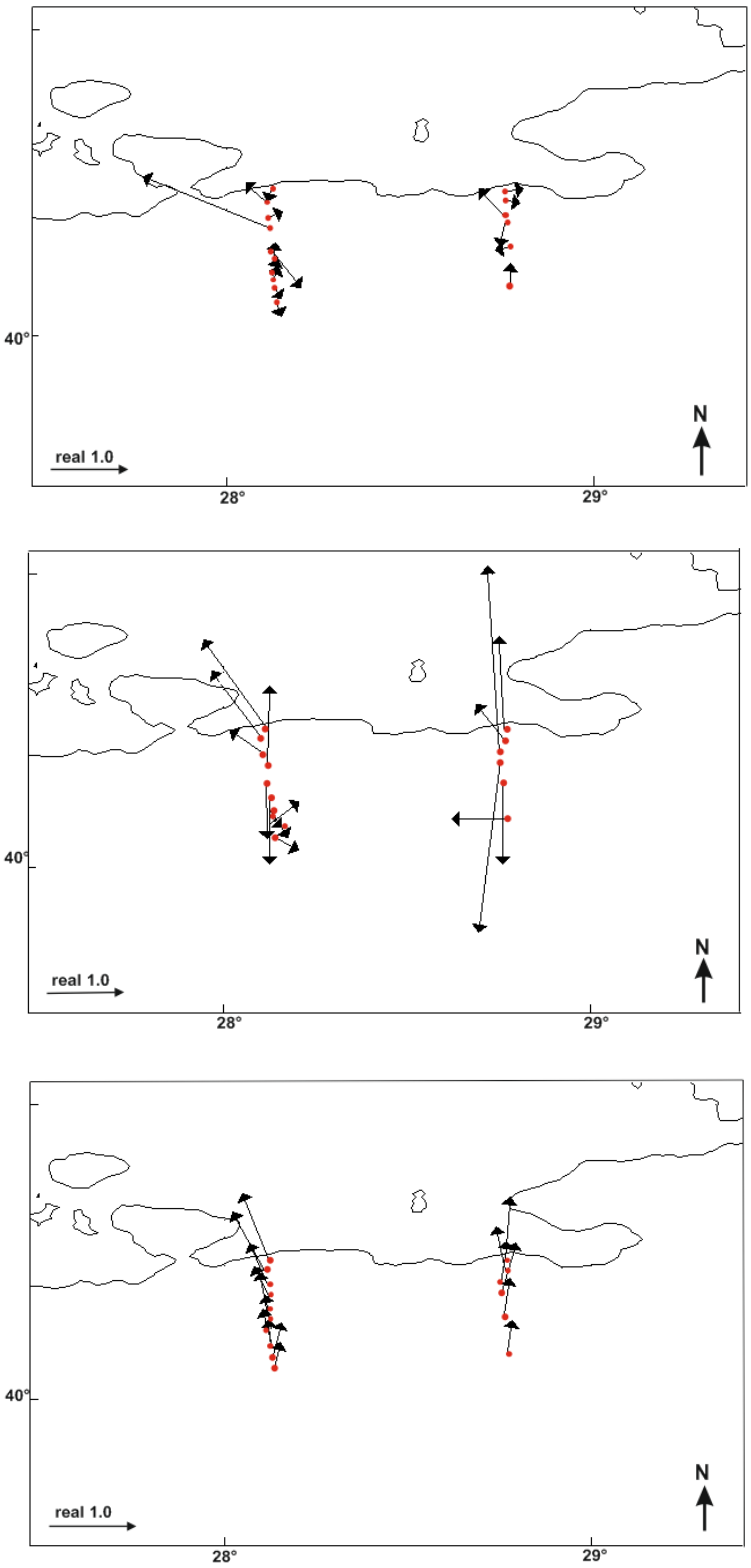

Figure 5.6. Real induction vectors (Parkinson convention (1962)) at three different frequencies 120 Hz, 0.1 Hz and 0.01 Hz

5.2. MT Sounding Curves

The apparent resistivity and phase curves depend on the geoelectric strike direction in the 2D Earth. In this respect, the distortion free impedance tensor obtained as a result of tensor decomposition must be rotated from the field coordinate frame to the geoelectric strike in order to define electrically polarized (TE) and magnetically polarized (TM) modes. In the data processing, the optimal rotation angle was decided with the help of the results of multi-site-multi-frequency tensor decomposition, and the TE and TM modes were thus defined.

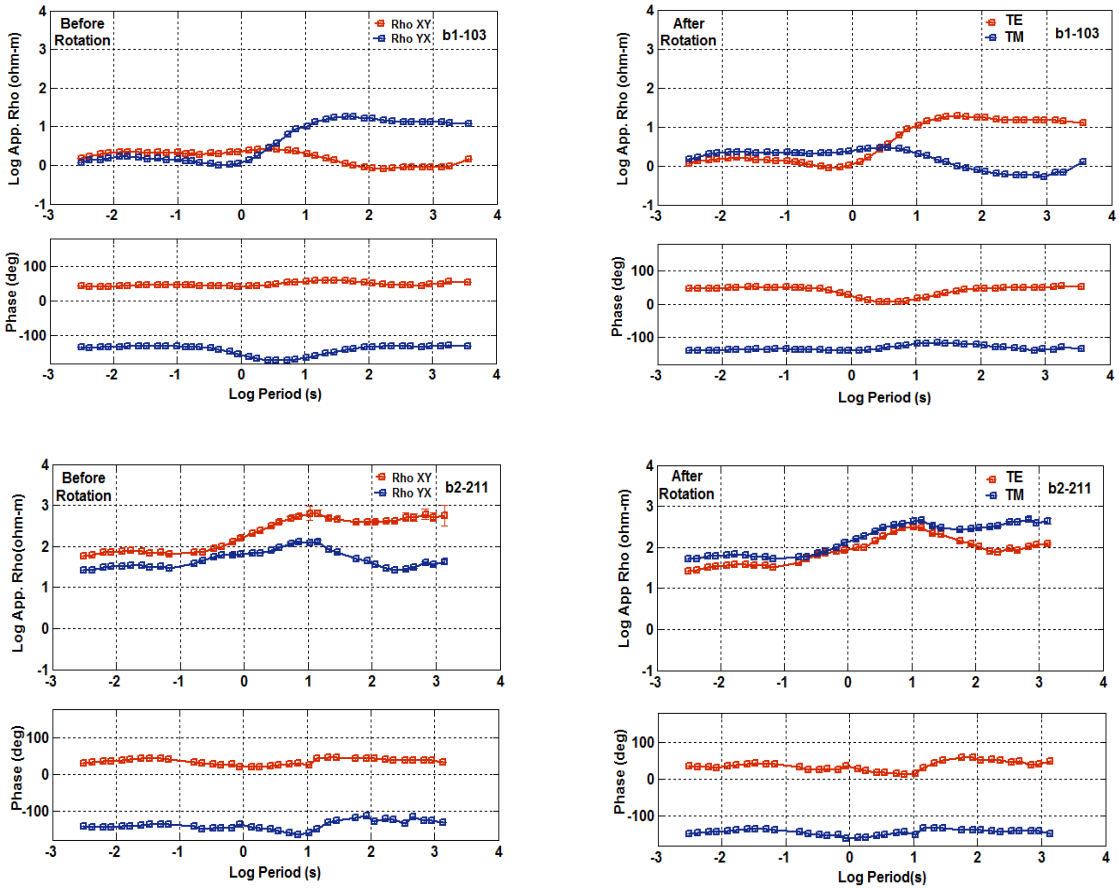

Figure 5.7. Comparison of apparent resistivity and phase curves before and after tensor decomposition for sample station from the PW (upper) and PE (bottom) profiles

XY and YX modes apparent resistivity and phase responses are termed as TE and TM modes after rotation of the data. Figure 5.7 shows examples of apparent resistivity and phase curves before and after rotation for sample stations of PW and PE profiles. It can be seen clearly that there is almost exchange between the data before and after rotation owing to dominantly 2D regional structure.

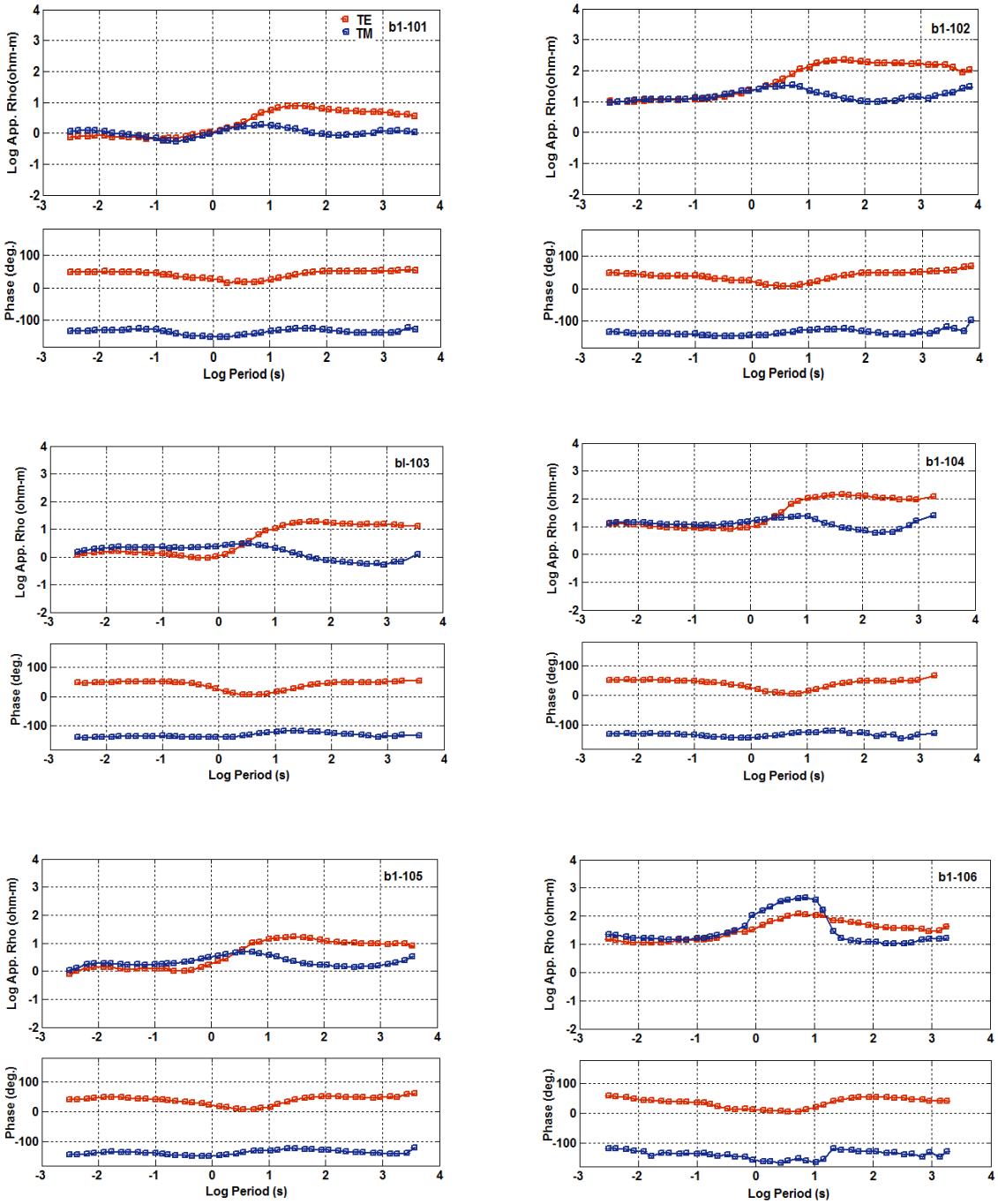

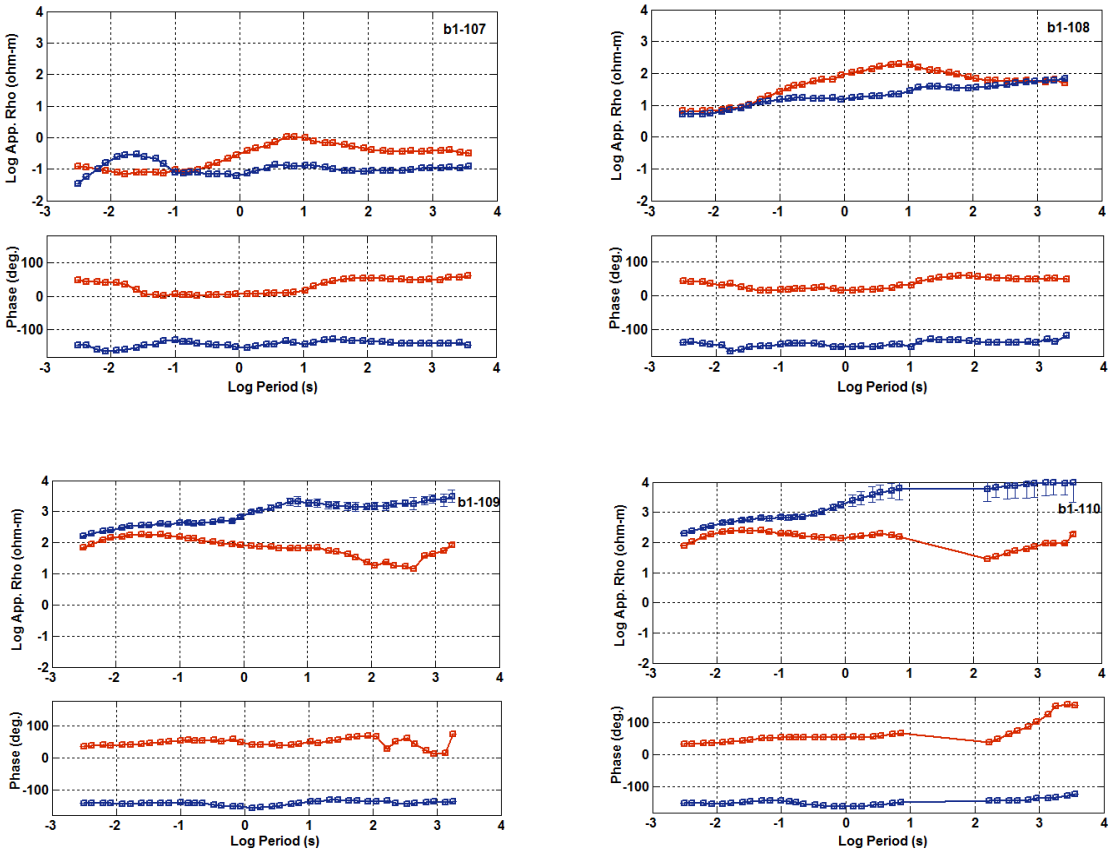

Figure 5.8. Apparent resistivity and phase curves after decomposition and rotation of stations from the PW profile that is in the direction of geoelectric strike. TE mode data are shown in red and TM mode data are shown in blue

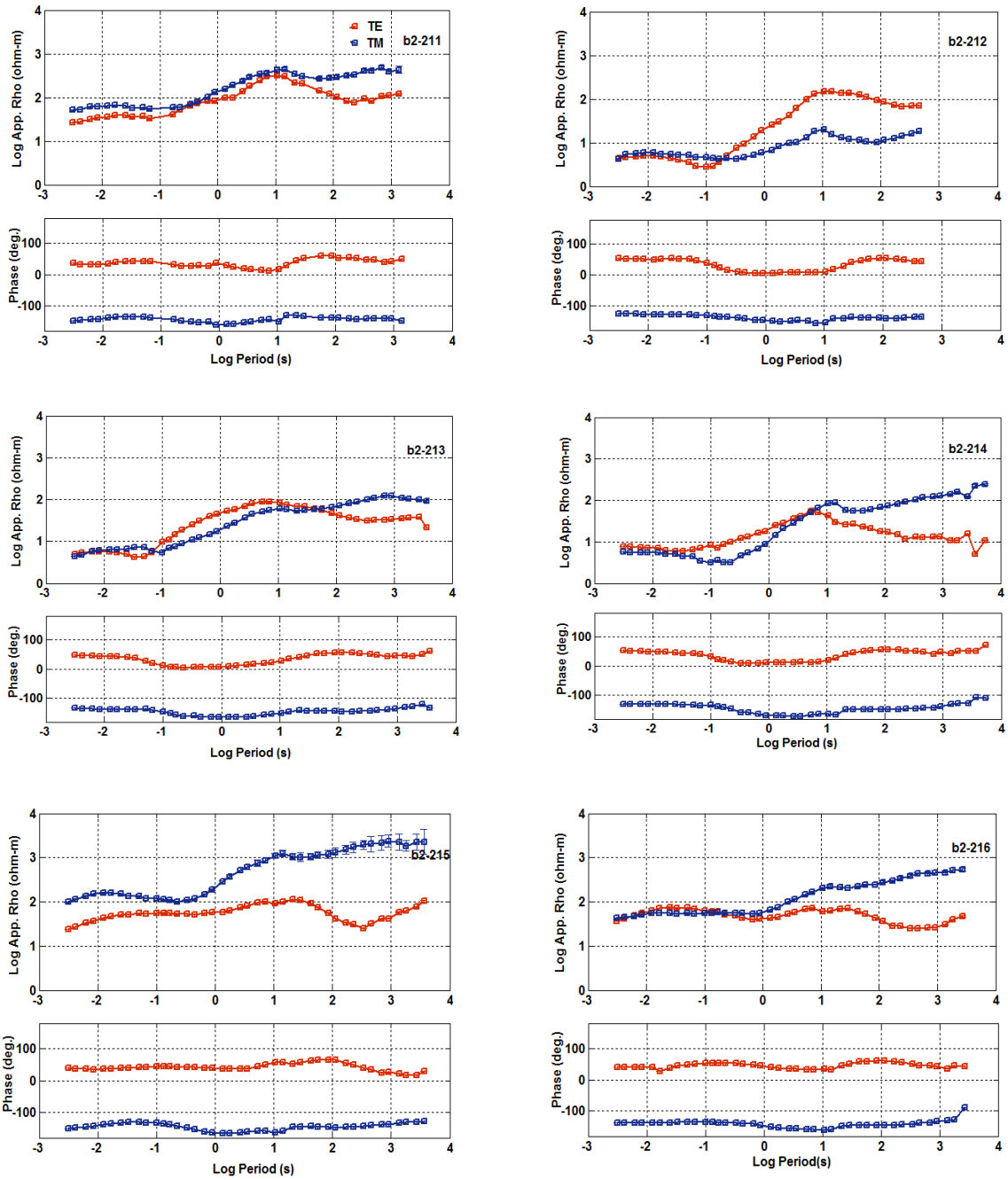

Figure 5.9. Apparent resistivity and phase curves after decomposition and rotation of stations from the PE profile that is in the direction of geoelectric strike. TE mode data are shown in red and TM mode data are shown in blue

Figure 5.8 and 5.9 exhibit the MT sounding curves after rotation for all stations of PW and PE profiles, respectively. The smooth apparent resistivity and phase curves with error bars represent the high quality of the MT data in all of the sounding curves. The apparent resistivity and phase curves at longer periods are split for all sites except the station b1-108 which has 1D character for these periods. At short periods, the overlap of the TE and TM mode apparent resistivity and phase curves for almost all sites show 1D character of the sounding medium. However, several stations b1-107, b1-109, b1-110 for the PW and b2-211, b2-215 for the PE profiles at short periods demonstrate splitting owing to the effect of the near surface inhomogenities known as galvanic distortion.

While the coast effects lead to high phases and low apparent resistivities in the TE mode, low phases and high apparent resistivities are observed in the TM mode. In the PW profile, the stations b1-110 and b1-109 which are 1.1 and 4.0 km inland from the Marmara Sea, respectively, show such characters on the TE and TM mode apparent resistivity and phase curves. In the PE profile, the stations b2-216 and b2-215 which are 1.4 and 4.4 km inland from the Marmara Sea, respectively, also exhibit the same peculiarities on the sounding curves. The resistivity of seawater (0.25 Ωm) was set into the initial model in order to overcome the possible artifacts of such effects on the final model in the modeling.

In south Marmara region, the TE mode apparent resistivity curves for the stations b1-101, b1-102, b1-103 and b1-104 show similar pattern, with constant apparent resistivity at short periods and an increase above 1s, which is an indicator of two resistivity layers beneath these stations that are located in the southern part of the PW profile. The stations b1-105, b1-106, b1-107 and b1-108 also have similar pattern at short periods, and the behavior of curves at longer periods characterizes a third resistivity layer. The TE mode apparent resistivity curves at all stations from the PE profile also indicates similar resistivity structure in the apparent resistivity curves.

5.3. 2D Inversion of MT Data

The apparent resistivity and phase data were inverted to obtain true resistivity model. An initial resistivity model was generated in order to compute the predicted MT data. The relationship between the responses of model and measured data were then searched by an inversion scheme. The agreement between predicted and measured data was controlled by model parameters, and the initial model was modified iteratively until the resistivity models which fit the measured data were obtained.

The south Marmara data was inverted by utilizing two-dimensional inversion code developed by Ogawa and Uchida (1996). By using the code, the smoothest models were searched while minimizing the misfit between measured data and model response. The apparent resistivity and phase data were used to perform 2D inversion for TE and TM modes (as well as TE+TM joint inversion). The electrical resistivity of the uniform Earth of 100 Ωm was taken as an initial model for both profiles. The mesh was designed with rectangular cells 84 columns wide and 58 rows depth for the PW, and 78 columns wide and 61 rows depth for the PE profiles. While the center of mesh is dense, cell thickness and width gradually increase further away. The resistivity of Marmara Sea (0.25 Ωm) (as a constraint) was fixed into the northern end of the models in order to overcome the coast effects.

Static shift is also taken into account as a constraint in the code, and thus the effect of it is minimized during the inversion. There are some other ways to minimize the effects of frequency independent shift of the apparent resistivity (static shift). These are special filtering, constraints from other geophysical methods such as well-logging, DC resistivity and time domain sounding as well as the MT data, the introduction of a larger error for apparent resistivity compared with the phase in the inversion (Ogawa, 2002).

Table 5.1. Inversion parameters used to obtain the smoothest and best fitting models (bold and italic) for both profiles

Model inversion parameters for the PW and PE profiles	
Input data	Apparent resistivity and phase data for ***TE*** and ***TM*** modes
Frequency range	***320-0.0005 Hz***
Error floor	***10*** per cent for apparent resistivity and ***2.86***° for phase
Smoothing parameter (α)	1, 2 ,3, 5, ***7***, 8, 10, 15, 20, 25, 30, 35, 40, 45, 50, 70, 80,100
Static shift parameter (β)	1, 3, 5, 7, ***10,*** 15, 20, 25, 30, 35, 40, 45, 50, 70, 80, 100
Weighting function (w)	***1***
Iteration No.	***28***
r.m.s.	***2.80*** for PW and ***2.08*** for PE

In the inversion process, all available frequencies were used and many combinations of model parameters were tried to generate the smoothest models which fit the south Marmara data. The smoothest models can be achieved by taking the larger values of smoothing parameter. However, an increase in the smoothing parameter gives rise to higher r.m.s. misfit that describes the differences between the measured data and model response. The inversion parameters used to invert the south Marmara data are given in the Table 5.1.

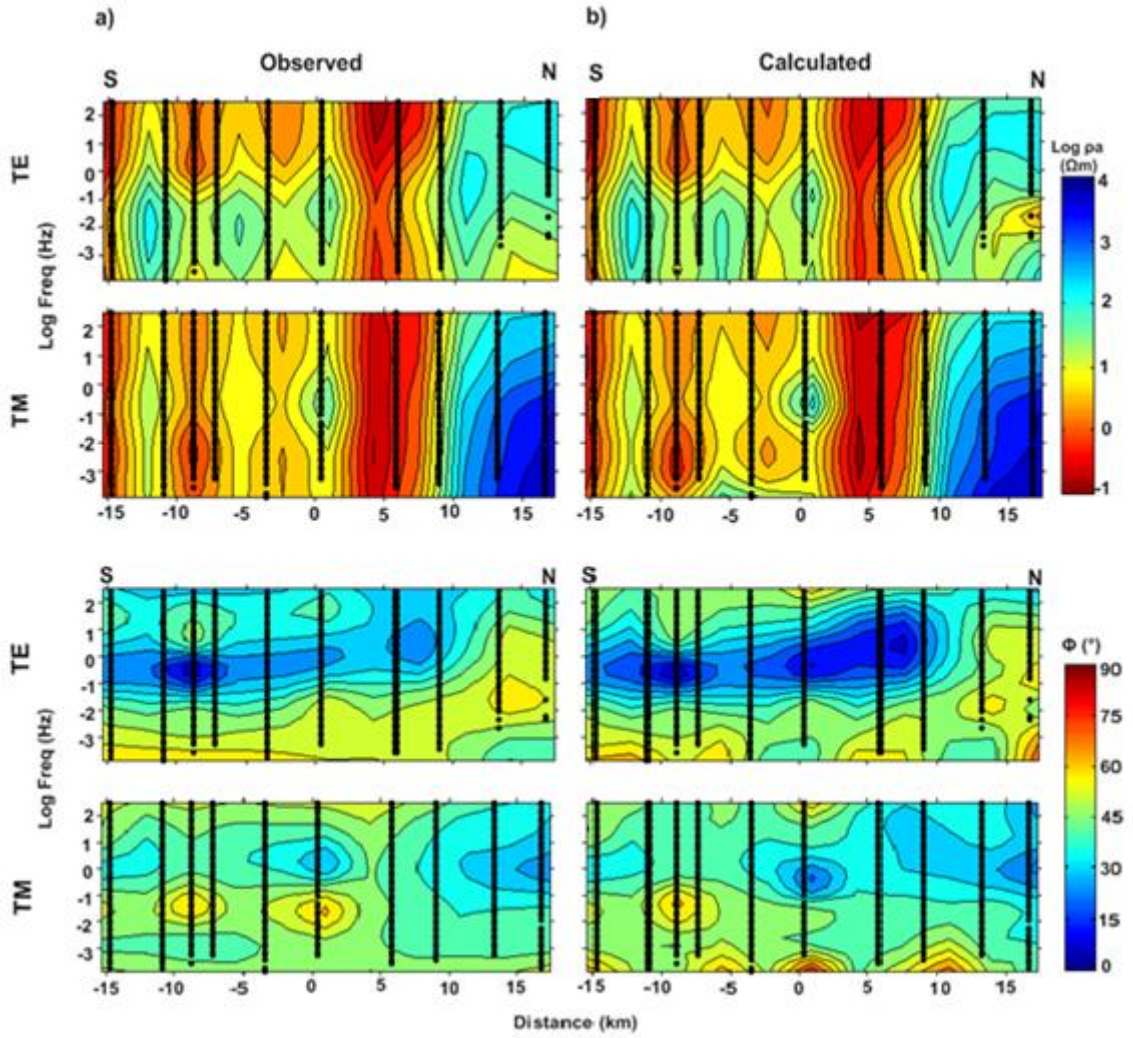

Figure 5.10. Observed and calculated apparent resistivity and phase pseudosections for the PW profile. a) Observed apparent resistivity (upper two) and phase (bottom two) pseudosections of TE and TM modes, respectively, from the top to the bottom. b) Calculated apparent resistivity and phase pseudosections in the same notation as (a). Small dots indicate different frequencies

Pseudosections of apparent resistivity and phase of impedance for observed and calculated data for the PW and PE are displayed in Figures 5.10 and 5.11, respectively. The electrical resistivity transition in different tectonic structures can be clearly seen in pseudosections. The pseudosections of observed data (Figures 5.10-a and 5.11-a) on both profiles seem to be in good agreement with the pseudosections of calculated data (Figures 5.10-b and 5.11-b).

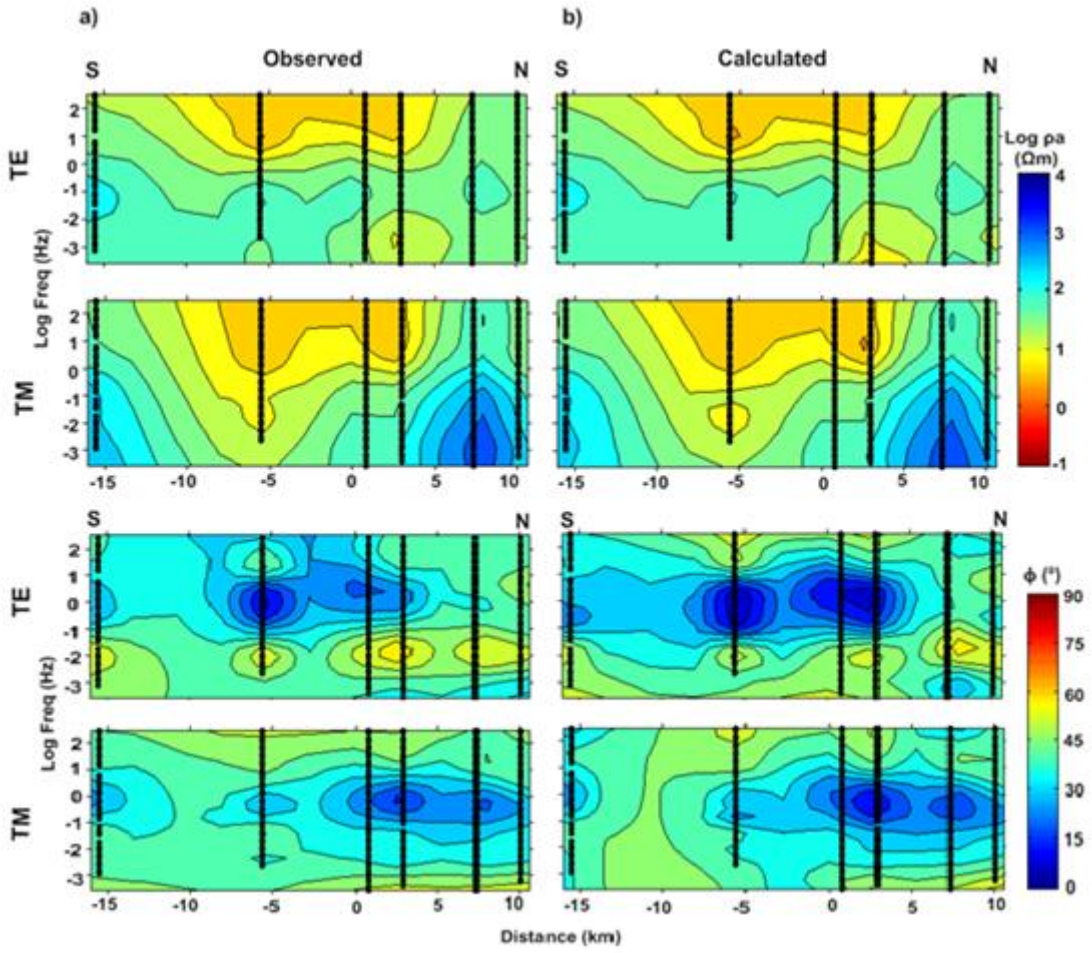

Figure 5.11. Observed and calculated apparent resistivity and phase pseudosections for the PE profile. a) Observed apparent resistivity (upper two) and phase (bottom two) pseudosections of TE and TM modes, respectively, from the top to the bottom. b) Calculated apparent resistivity and phase pseudosections in the same notation as (a). Small dots indicate different frequencies

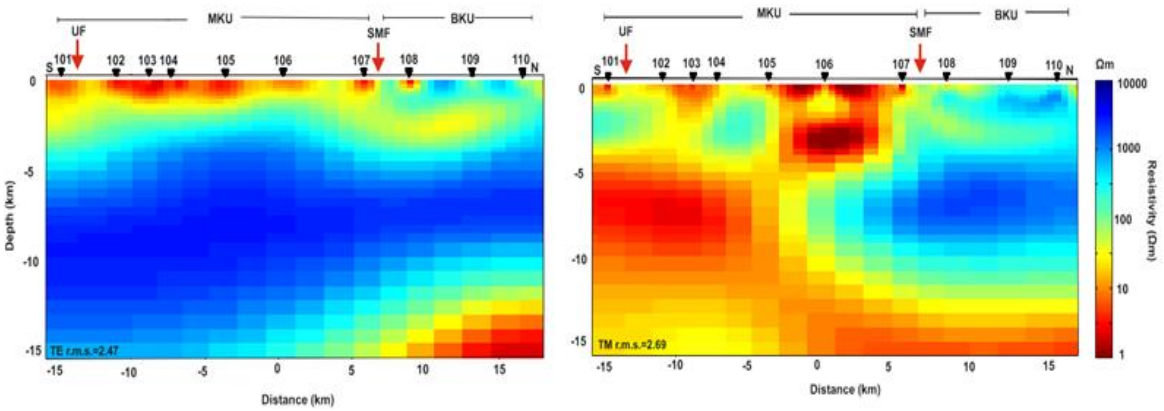

Figure 5.12. Final resistivity models derived for the PW profile with 2D inversion of the TE (left) and TM mode (right) data. Black triangles at the surface indicate the location of MT stations. The r.m.s. misfit is displayed in the bottom left corner of the model. MKB: Manyas-Karacabey basin, BKU: Bandırma-Karadağ uplift, UF: Uluabat fault, SMF: South Marmara fault

Figure 5.12 demonstrates the model results from 2D inversion of the PW profile for the different inversion processes, TE (left) and TM mode (right) inversions. The geoelectric models developed from TE and TM mode data indicate two major conductors: a thin conductor with thickness changing along the profile at shallow depth and a second conductor at greater depths (>13 km). These two conductors also exist on the model derived from joint inversion of the TE and TM mode data (Figure 5.13-b). The deeper conductor is much clear in the model derived from TE mode data because TE mode is more sensitive to deep structures than TM mode (Berdichevsky *et al.*, 1998). Additionally, two resistors coincide with on the north end of the models. The shallow resistor at depth less than 2 km and the deeper resistor at depth ~4-10 km are present. These features are also clear on joint inversion of TE and TM mode data (Figure 5.13-b).

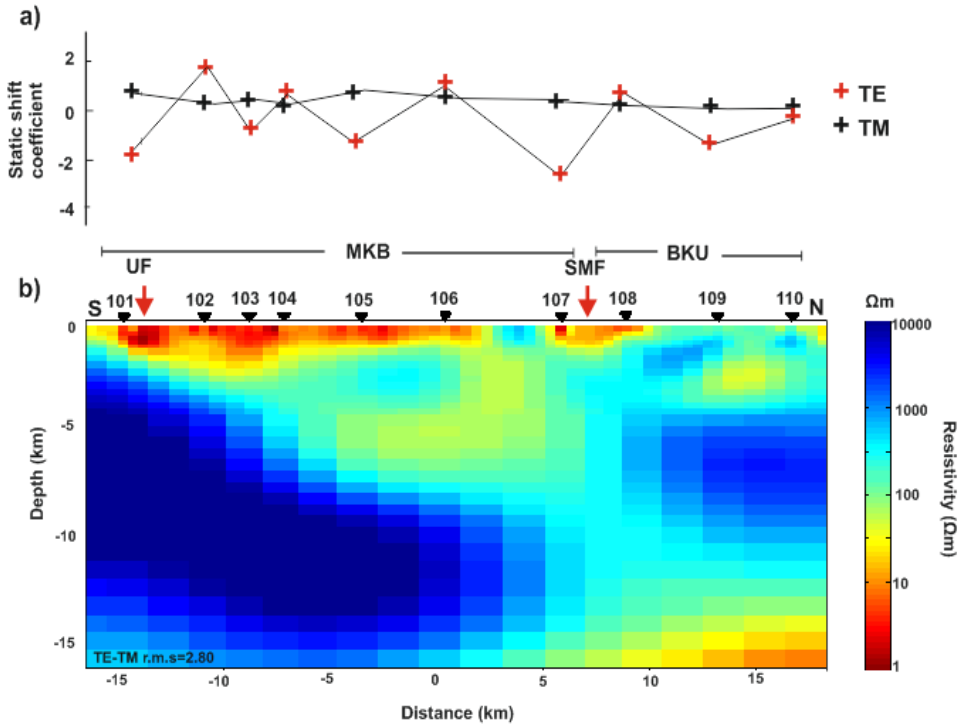

Figure 5.13. a) The static shifts as a function of location for TE and TM modes, b) Final resistivity model derived for the PW profile with 2D inversion of the TE and TM mode data. Black triangles at the surface indicate the location of MT stations. The r.m.s. misfit is displayed in the bottom left corner of the model. MKB: Manyas-Karacabey basin, BKU: Bandırma-Karadağ uplift, UF: Uluabat fault, SMF: South Marmara fault

The static shift coefficients of the stations along the PW profile for the TE and TM modes are displayed in Figures 5.13-a. The TM mode is almost undistorted, but the TE mode is affected by the static shift (Figure 5.13-a). The changes in the value of the static shift coefficients are associated with superficial 3D bodies. Figures 5.13-b illustrates the optimal resistivity model constructed from joint inversion of the TE and TM mode data for the PW profile. This model indicates a strong conductor at the deepest part of the model. Two strong resistors on the both side of the model exist. There is also a relatively resistive zone between these two resistors in the model.

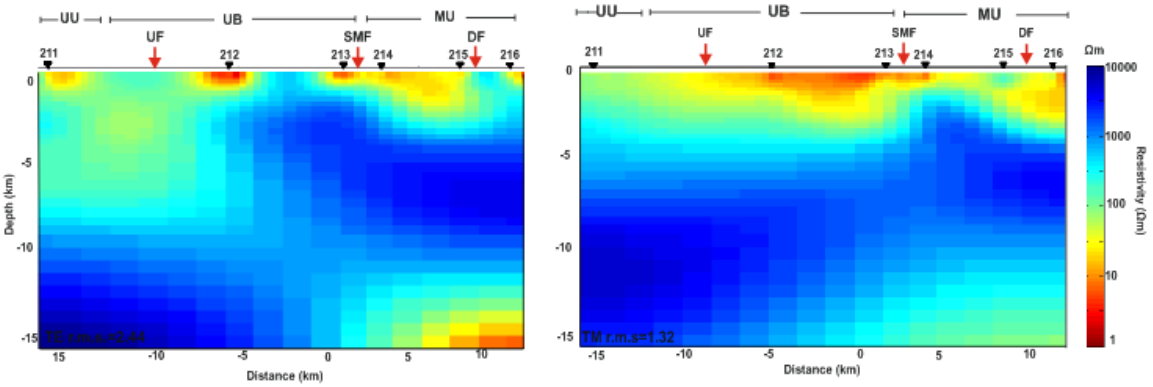

Figure 5.14. Final resistivity model derived for the PE profile with 2D inversion of the TE (left) and TM mode (right) data. Black triangles at the surface indicate the location of MT stations. The r.m.s. misfit is displayed in the bottom left corner of the model. UU: Uludağ uplift, UB: Uluabat basin, MU: Mudanya uplift, UF: Uluabat fault, SMF: South Marmara fault, DF: Dereköy fault

Figure 5.14 displays the model results from 2D inversion of the PE profile for the different inversion processes, TE (left) and TM mode (right) inversions. The geoelectric models obtained from inversion of TE and TM mode data contain a conductor with thicknesses varying along the profile at shallow depth. Another conductor at the deepest part of the model derived from the TE mode is present, and the model developed from TM mode data includes a relatively conductive layer at corresponding depth. These conductors are also shown on the model obtained from the TE+TM joint inversion (Figure 5.15-b). Moreover, resistors existing on the both side of the models are present the model developed using joint inversion of the TE and TM mode data (Figure 5.15-b).

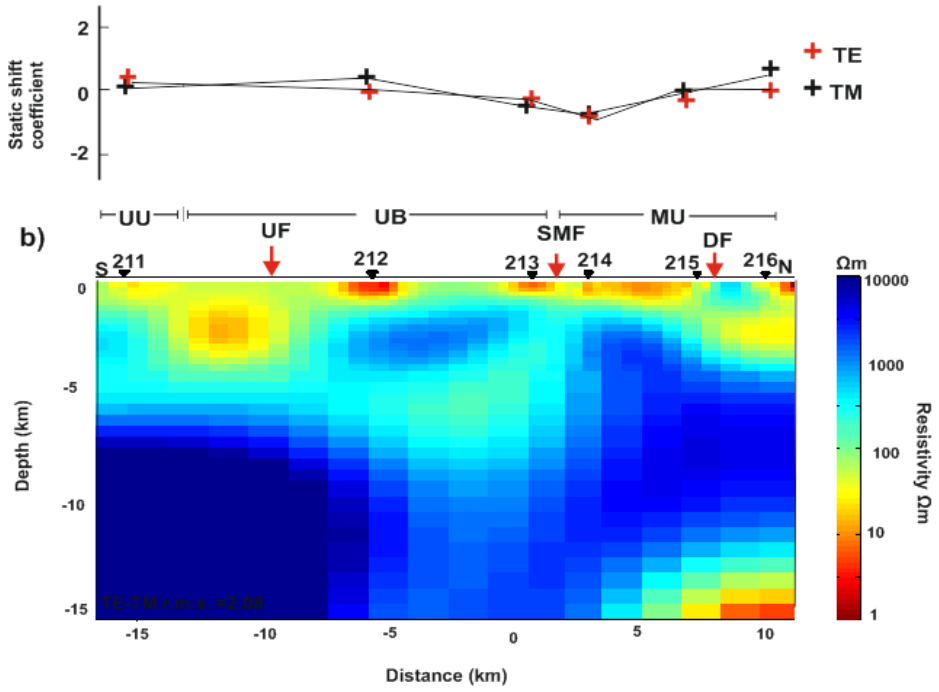

Figure 5.15. a) Static shifts as a function of location for TE and TM modes, b) Final resistivity model derived for the PE profile with 2D inversion of the TE and TM mode data. Black triangles at the surface indicate the location of MT stations. The r.m.s. misfit is displayed in the bottom left corner of the model. UU: Uludağ uplift, UB: Uluabat basin, MU: Mudanya uplift, UF: Uluabat fault, SMF: South Marmara fault, DF: Dereköy fault

The static shift estimates along the PE profile for the TE and TM modes are displayed in Figures 5.15-a. The TE and TM modes show almost the same rate of distortion by static shift (Figure 5.15-a). Figures 5.15-b illustrates the optimal resistivity model obtained from the joint inversion of the TE and TM mode data for the PE profile. A strong conductor at the deepest part of the model is shown. Except the shallow and deep conductive zones, the model includes strong resistors.

Both TE and TM mode apparent resistivity and phase data were used in the inversion to minimize the deficiency of one mode over the other (Berdichevsky *et al.*, 1998). Figures 5.13-b and 5.15-b illustrate the optimal resistivity models for PW and PE profiles, respectively. When compared, both inversion models show similarities at depths greater than ~5 km and differences at shallower depths. The TE+TM joint inversion

models of both parallel profiles indicate a strong conductor with resistivity of around 10 Ωm at the deepest part of the models, which is the prominent feature of both of the models. In addition to that, two strong resistors with resistivity greater than 1000 Ωm appear on the both sides of the models.

Figures 5.16 and 5.17 illustrate the response of apparent resistivity and phase from the joint inversion of TE and TM mode data of the PW and PE profiles, respectively. The apparent resistivity fits are better than the phase fits in most stations. The stations b1-109, b10-110 for the PW and b2-211, b2-214 for the PE profile show well fitting to TM mode, but the fit is poor to TE mode.

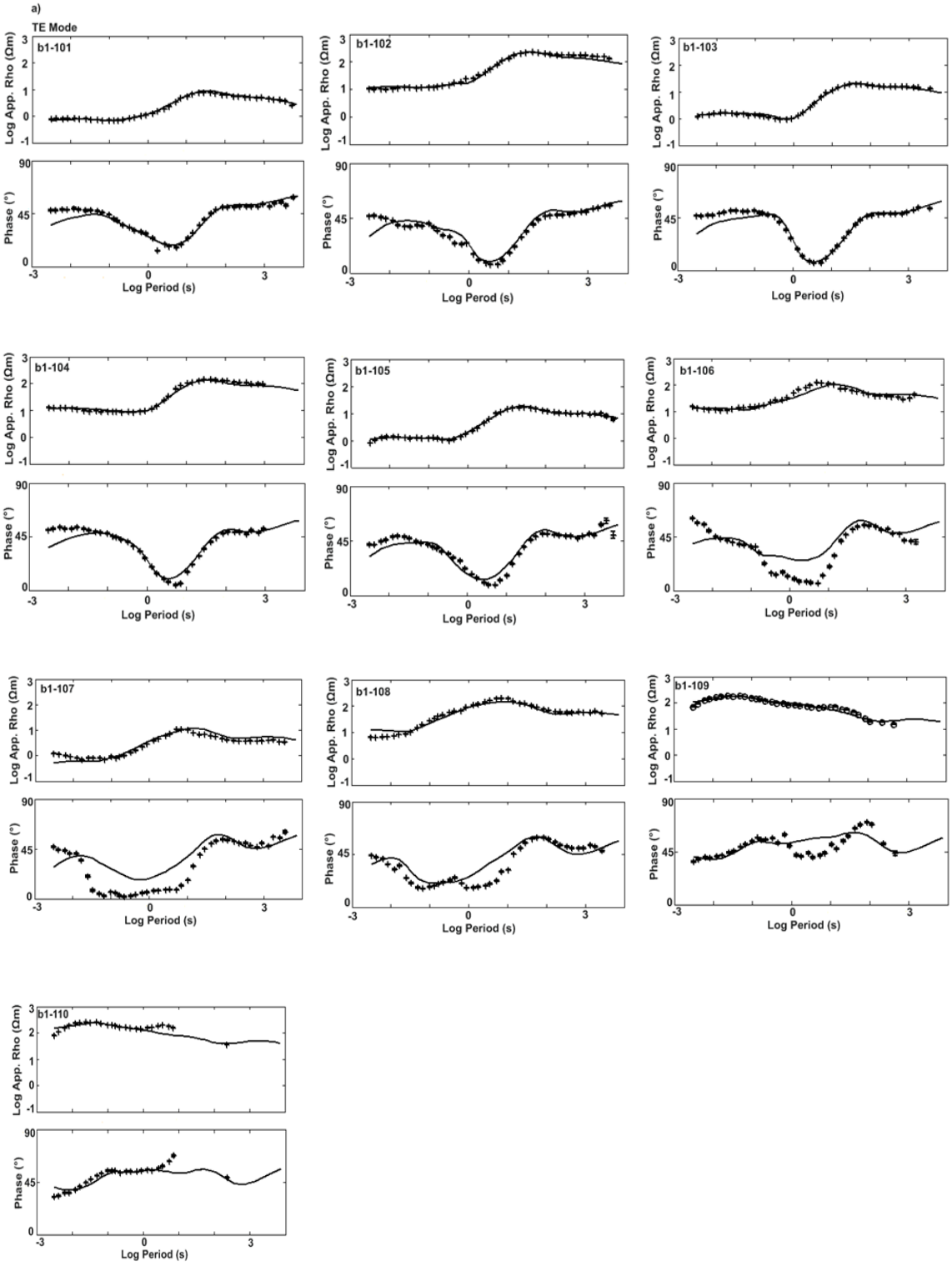
a)
TE Mode
b1-101
b1-102
b1-103
b1-104
b1-105
b1-106
b1-107
b1-108
b1-109
b1-110
Log App. Rho (Ωm)
Phase (°)
Log Period (s)
Log Perod (s)

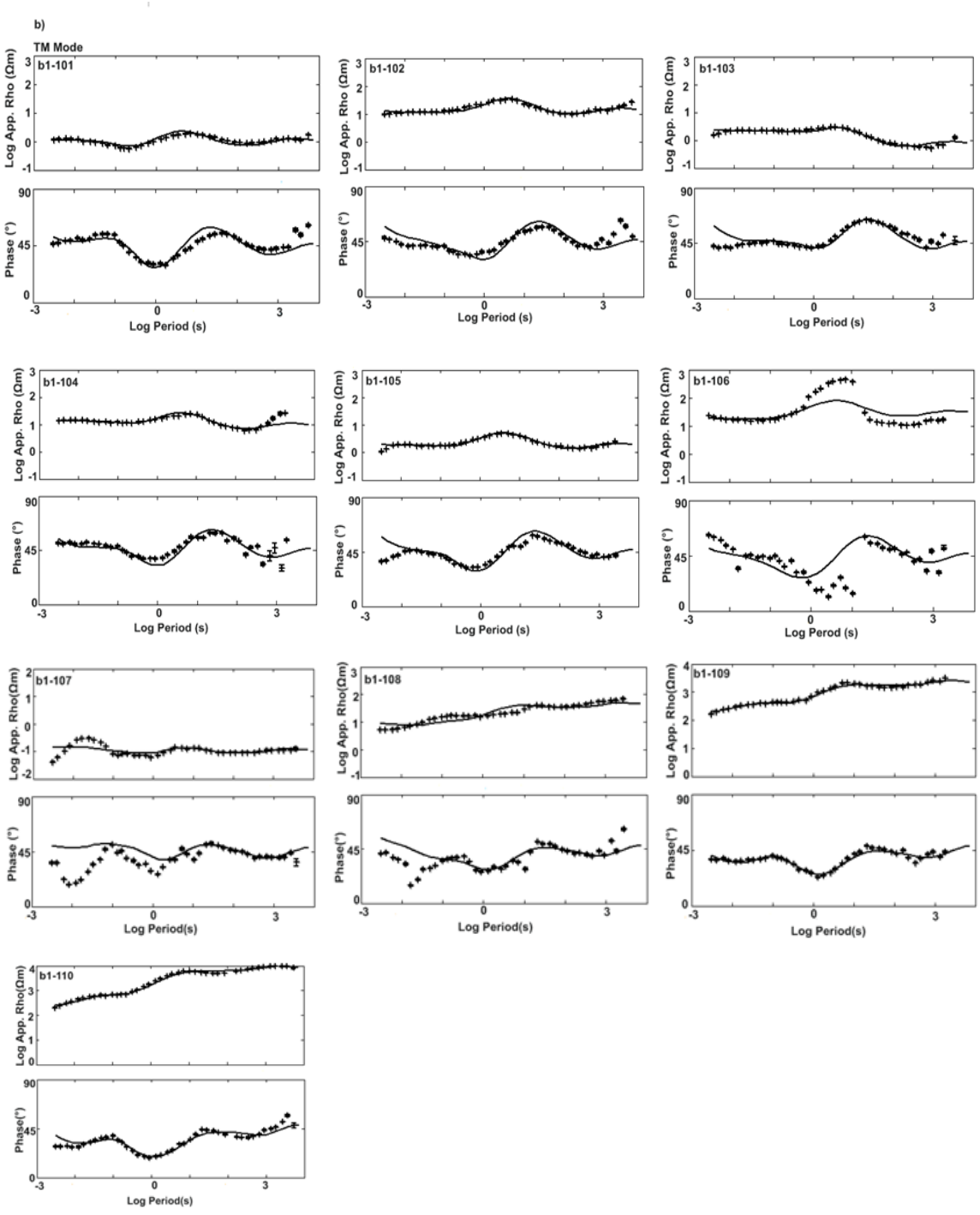

Figure 5.16. Fitting curves of observed and calculated data obtained from joint inversion of TE (a) and TM (b) modes of the PW profile. Solid lines represent the model response whereas plusses with error bars demonstrate the observed data

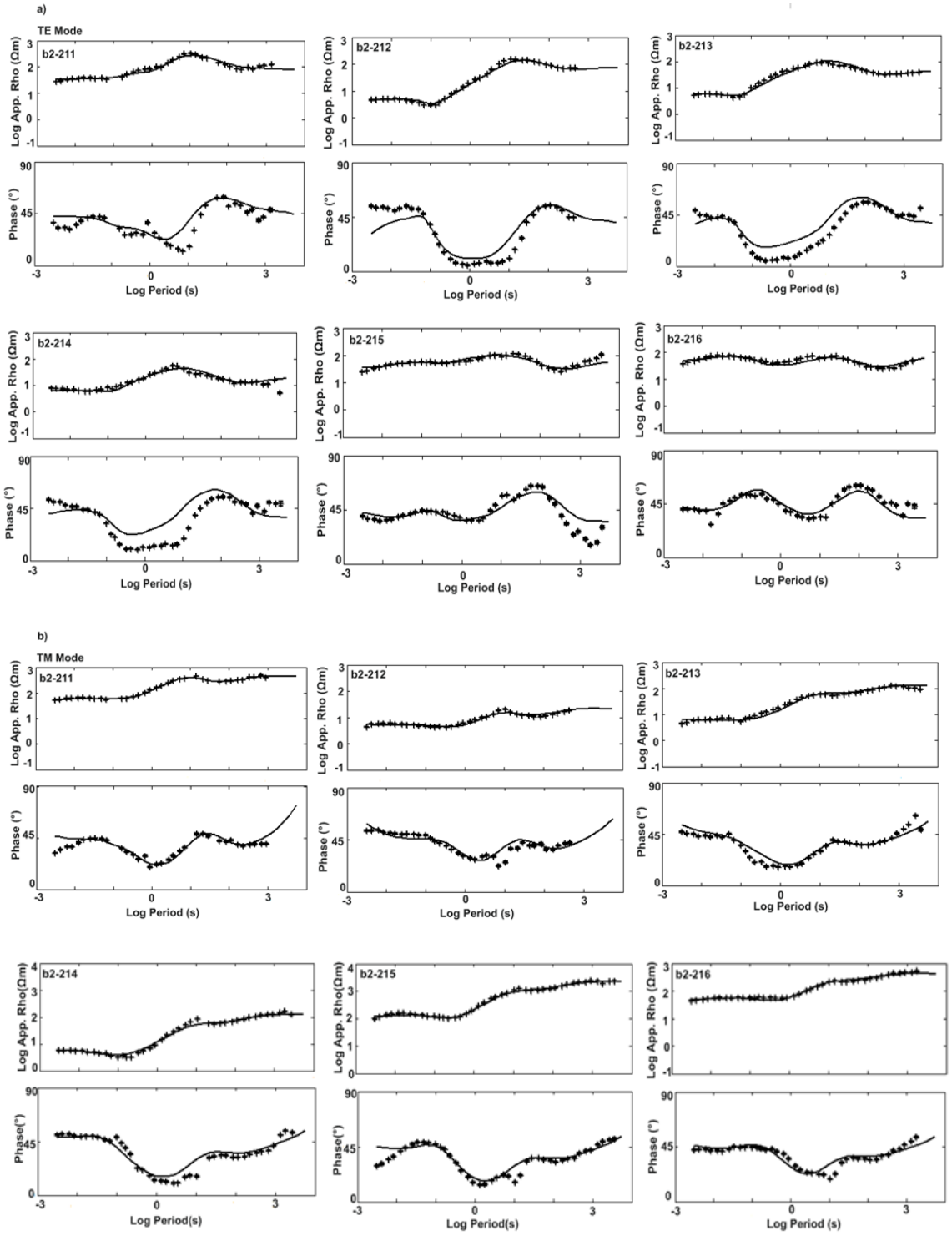

Figure 5.17. Fitting curves of observed and calculated data obtained from joint inversion of TE (a) and TM (b) modes of the PE profile. Solid lines represent the model response whereas plusses with error bars demonstrate the observed data

6. DISCUSSION

After obtaining the 2D geoelectric models of both profiles by using the joint inversion of TE and TM mode data, several tests were carried out to check the robustness of the final geoelectric models, shown in Figure 6.1, because it is important to make sure whether they are real or artifacts of the inversion process. The deep resistors and conductors on geoelectric models could not be real. Thus, it is significant to confirm if they are required by observed data before interpreting them.

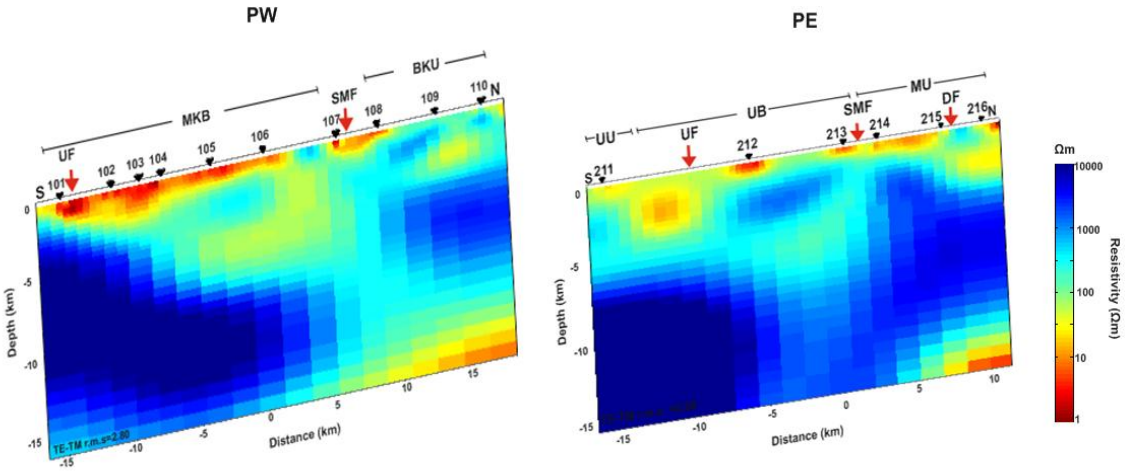

Figure 6.1. 2D resistivity models derived by inverting MT data. Black triangles at the surface indicate the location of MT stations. The r.m.s. misfit is displayed in the bottom left corner of the model. PW: West profile, PE: East profile, MKB: Manyas-Karacabey basin, BKU: Bandırma-Karadağ uplift, UU: Uludağ uplift, UB: Uluabat basin, MU: Mudanya uplift, UF: Uluabat fault, SMF: South Marmara fault, DF: Dereköy fault

6.1. Sensitivity Tests

6.1.1. Test-1

The first test was performed to the TE+TM mode geoelectric model for the PW profile (Figure 6.2). In this test, the high resistivity zone R1 was replaced by the conductive blocks of 10 and 500 Ωm (Figure 6.2). The sensitivity of observed data at these locations was tested by using forward modeling.

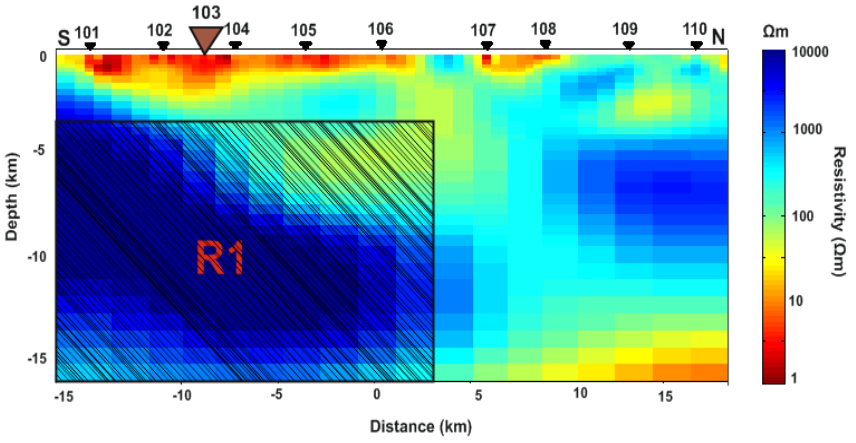

Figure 6.2. Geoelectric model for the PW profile obtained from 2D joint inversion of the TE and TM mode data. The deepest resistor is labeled as R1. R1 is replaced by the blocks with resistivity, 10 and 500 Ωm

Figures 6.3 shows the fitting curves of apparent resistivity and phase from the station b1-103 on the southern of the PW profile for the artificially inserted conductive (10 Ωm in pink and 500 Ωm in green) bodies. A station was selected over the deep resistor (R1) (Figure 6.2). While the forward response of the 500 Ωm block that was replaced by R1 indicates a worse fit to the TM mode data, the block with resistivity, 10 Ωm, shows a significantly worse fit to both modes. The worse fit yields that the extremely low resistivity

blocks to R1 are not appropriate to describe the subsurface electrical resisitivity structure of the study area.

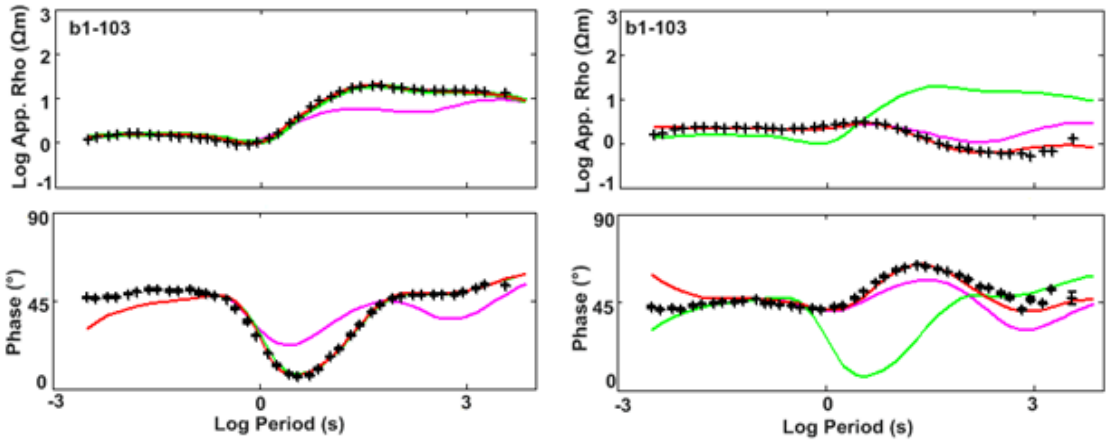

Figure 6.3. Apparent resistivity and phase curves of the TE (left) and TM (right) mode data at the station b1-103 located above R1. Observed data is shown by plusses. Red solid lines are the model response of the best fit model. Pink and green lines are the model response when R1 replaced by the resistive block of 10 Ωm and 500 Ωm, respectively

6.1.2. Test-2

In this test, the highly conductive zone C1 was tested (Figure 6.4). C1 was involved the geoelectric model constituted from the joint inversion of the TE and TM mode data for the PW profile. In this test, the strong conductor C1 was replaced with the resistive blocks of 500 and 1000 Ωm (Figure 6.4). The responses of the modified model in forward modeling were compared with the responses of the best fit model of the PW profile.

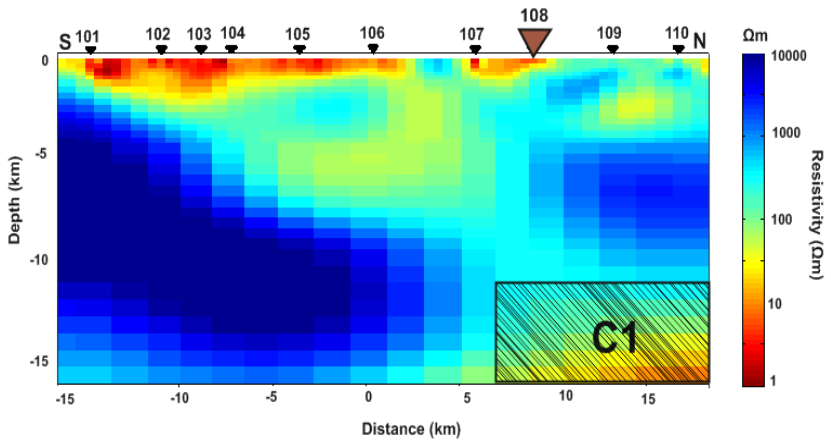

Figure 6.4. Geoelectric model for the PW profile obtained from 2D joint inversion of the TE and TM mode data. The deepest conductor is labeled as C1. C1 is replaced by the blocks with resistivity, 500 and 1000 Ωm

Figure 6.5 exhibits the fitting curves of apparent resistivity and phase from station b1-108 on the northern of the PW profile for the artificially inserted conductive (500 Ωm in green and 1000 Ωm in blue) bodies. A station was selected over the deep conductor (C1) (Figure 6.4). The forward responses at long periods indicate that the feature C1 is definitely required by both TE and TM mode data. The worse fit yields that the extremely high resistivity blocks of C1 are not appropriate to characterize the electrical resistivity structure of the study area.

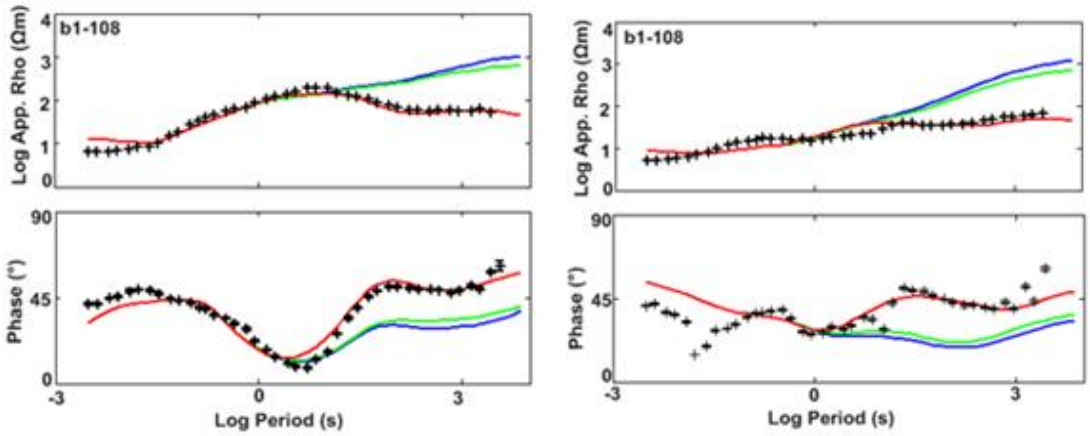

Figure 6.5. Apparent resistivity and phase curves of the TE (left) and TM (right) mode data at the station b1-108 located above C1. Observed data is shown by plusses. Red solid lines are the model response of the best fit model. Green and blue lines are the model response when C1 replaced by the resistive block of 500 and 1000 Ωm, respectively

6.1.3. Test-3

In this test, the highly resistive zone R2, which is shown in Figure 6.6, was tested. R2 is included from the geoelectric model obtained from the joint inversion of the TE and TM mode data for the PE profile. In this test, R2 was replaced by the conductive blocks of 10 and 500 Ωm (Figure 6.6). The sensitivity of the MT data was asserted to the existence of the artificial bodies by utilizing forward modeling.

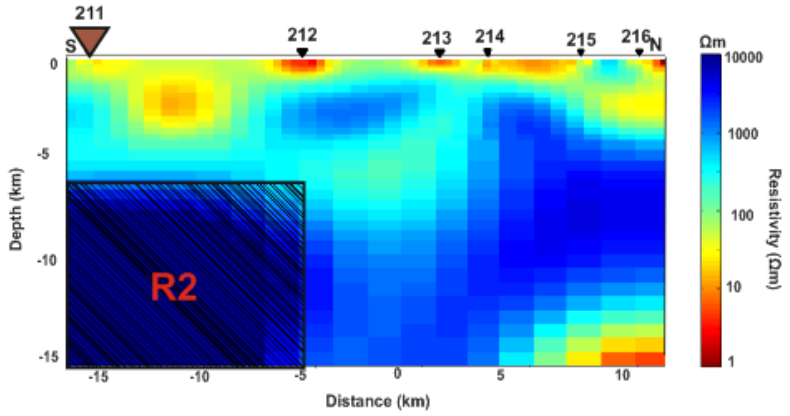

Figure 6.6. Geoelectric model for the PE profile obtained from 2D joint inversion of the TE and TM mode data. The deepest resistor is labeled as R2. R2 is replaced by the blocks with resistivity, 500 and 1000 Ωm

Figure 6.7 demostrates the fitting curves of apparent resistivity and phase from station b2-211 on the southern of the PW profile for the artificially inserted conductive (10 Ωm in pink and 500 Ωm in green) bodies. A station was selected over the deep resistor (R2) (Figure 6.6). Although the forward response of the 500 Ωm block shows a worse fit to the TM mode data, the block with resistivity, 10 Ωm, exhibits worse fit to both modes.

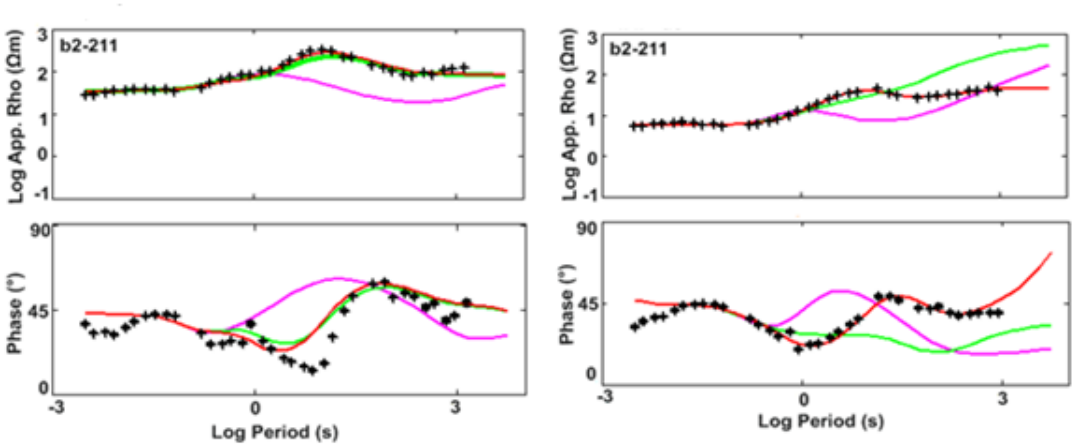

Figure 6.7. Apparent resistivity and phase curves of the TE (left) and TM (right) mode data at the station b2-211 located above R2. Observed data is shown by plusses. Red solid lines are the model response of the best fit model. Pink and green lines are the model response when R2 replaced by the resistive block of 10 and 500 Ωm, respectively

6.1.4. Test-4

The third test was performed to the TE+TM mode geoelectric model for the PE profile (Figure 6.8). In this test, the strong conductor C2 was replaced by the conductive blocks of 500 and 1000 Ωm (Figure 6.8). Calculating the responses of the modified models in forward modeling allowed comparing the fit of the responses of the best fit model of the PE profile with modified models.

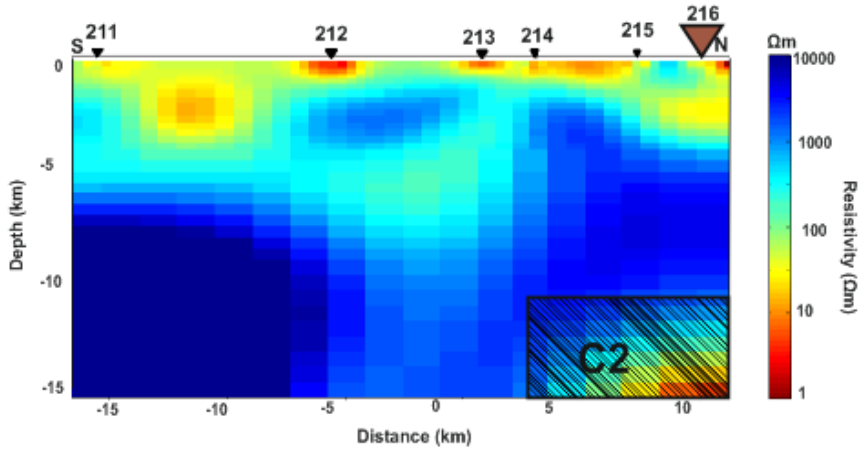

Figure 6.8. Geoelectric model for the PE profile obtained from 2D joint inversion of the TE and TM mode data. The deepest conductor is labeled as C2. C2 is replaced by the blocks with resistivity, 500 and 1000 Ωm

Figure 6.9 shows the fitting curves of apparent resistivity and phase from station b2-216 on the northern of the PE profile for the artificially inserted conductive (500 Ωm in green and 1000 Ωm in blue) bodies. A station was selected over the deep conductor (C2) (Figure 6.8). The forward responses at long periods indicate a dramatically worse fit to both TE and TM modes.

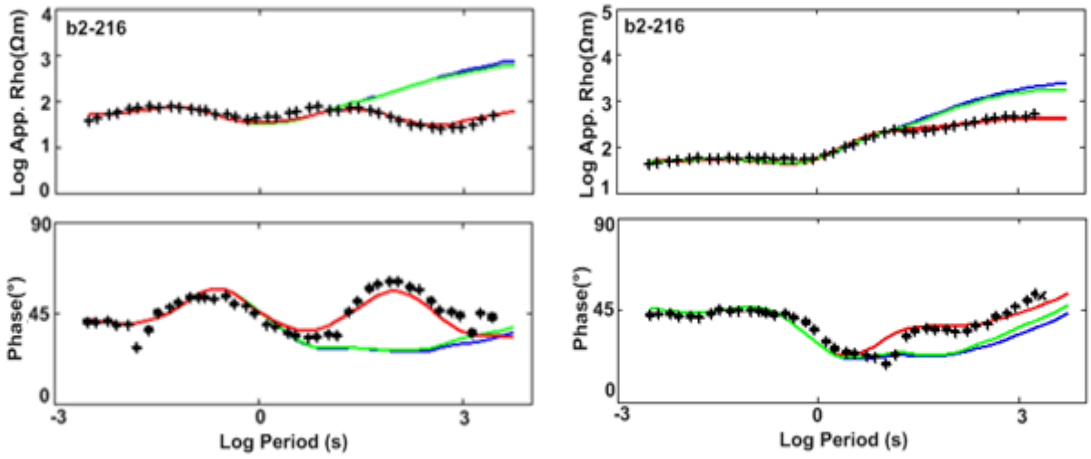

Figure 6.9. Apparent resistivity and phase curves of the TE (left) and TM (right) mode data at the station b2-216 located above C2. Observed data is shown by plusses. Red solid lines are the model response of the best fit model. Green and blue lines are the model response when C2 replaced by the resistive block of 500 and 1000 Ωm, respectively

The forward responses at long periods indicate a dramatically worse fit to the response of the models, which suggests that the features R1, C1, R2 and C2 are definitely required by the TE and TM mode data. Therefore, the models with tested deep resistors and conductors are appropriate to represent the observed data and thus subsurface electrical resistivity structure of the south Marmara region.

6.1.5. Other Tests

To justify the geoelectric models, MT data were inverted with a starting model of 1000 Ωm in addition to 100 Ωm homogeneous half space. A wide range of error floors to apparent resistivity and phase data were also tried during the inversions. Moreover, inversions were performed except the station b1-107. Since the station b1-107 has low resistivity values in contrast to the adjacent stations b1-106 and b1-108, the deep strong resistor (R1) may be an artifact of this high contrast. The results of these tests are not

presented. The comparison of all inversion outcomes confirms the distinct zones, R1, C1, R2 and C2.

6.2. Interpretation

The relationship between geoelectric models and geological state is significant to assess the subsurface conductivity structure that is constituted from 2D modeling of MT data. The evaluation of geoelectric models also requires additional information derived from utilizing different geological and/or geophysical methods.

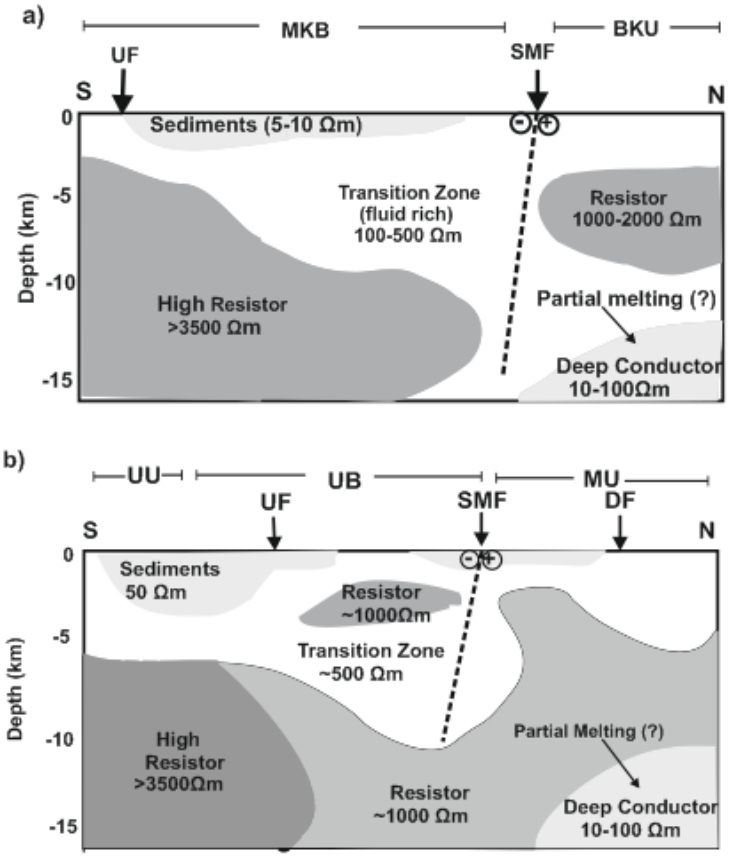

Figure 6.10. Cartoon sketch showing possible interpretation for the PW (a) and PE profiles (b). The broken lines are faults. + and - represent the movement direction of the walls of the faults

The geometry of different geological and lithological regions was defined to the depths of less than 16 km. The interpretive cross-sections based on the geoelectric models are presented in Figure 6.10. These models have similar electrical resistivity patterns. In these models, crust is presented by blank areas and faults are represented by broken lines. These parts of the geoelectric models have high conductivity value, which is why they explained by fluid rich region or partially melted areas in the crust. The shallow conductor located on the southern end of the models suggested as sedimentary fill. The shallow conductors along the SMF are explained as fracture zones. The uplift and depression areas in the models are bounded by SMF. Two strong resistors on the both sides of the models are associated with low fluid condition in the crust.

The conductivity structure of the crust paves the way to characterize the mechanically weak zones which are related to fluids in the crust. The existence of fluids in the crust may perturb the long term structural and compositional evolution of the fault zones and change the local stress regime in the area (Zhao *et al.,* 1996). The changing stress regime owing to fluids may drive the fault zones mechanical failure in seismogenic zones. High conductivity zones (C1 and C2) associated with the presence of fluids in the crust of the southern Marmara also lead to mechanically weakening of the crust, and they may trigger the seismic activity in the region. Therefore, the role of fluids in tectonically active southern Marmara region is strongly related to the geoelectrical properties and dynamics of the region.

The geoelectric strike of N102°E and N72°E in the south Marmara region were calculated for the PW and PE profiles, successively, by utilizing the multi-site-multi-frequency tensor decomposition analysis for all sites over the whole frequency band. These values of geoelectric strikes show a good correlation with the NE-SW trending structural features of the regional geology (Okay *et al.,* 1991; Yılmaz *et al.,* 2010). In this way, it can be suggested that the geoelectric models aligned along those strike directions confirm the regional geology.

The 2D inversion of MT data results in models which agree well with the regional morphology, stratigraphy, and tectonics. The southern part of the study area is located on the southern branch of NAF. The uplift and depression areas in the region are dominated by this branch of the NAF (Selim *et al.,* 2006). Some of these areas, Manyas-Karacabey basin and Bandırma-Karadağ uplift on the model derived from the PW profile, and Uluabat basin, Mudanya and Uludağ uplifts on the model obtained from the PE profile, can be clearly shown in the geoelectric models (Figure 6.1). The regional morphology on the region is also controlled by the NE-SW trending right lateral and strike slip dominant faults (Gürer *et al.,* 2003; Selim *et al.,* 2006; Yılmaz *et al.,* 2010). Some of the faults crossed by MT lines are located in the relatively resistive (~500 Ωm) transition zones. Thus, the lateral variations of electrical conductivity in the region may be dominated by these faults or lateral variations of formations.

The TE+TM joint mode inversion models indicate two strong resistors with resistivity greater than 1000 Ωm on the both side of the models. These resistors can be associated with Precambrian rocks due to the fact that the basement of the Sakarya Continent is formed by these units (Selim *et al.,* 2006). These resistors are related to low fluid conditions and high rigidity in the crust.

A shallow conductor located on the southern end of the models from surface to ~3-4 km depth may associate with sedimentary fills. Sediments may fill depending on the local stress regime in the area. These areas coincide with Manyas-Karacabey basin on the PW profile and Uluabat basin on the PE profile. These basins are pull-apart basins and formed by NE-SW trending extensional stress regime (Selim *et al.,* 2006). The shallow conductors along SMF are also interpreted as fracture zones.

A strong conductor with resistivity around 10 Ωm at the deepest part of the models also exists. High values of conductivity at these depths can be due to the presence of fluids in the crust, partial melting and/or a combination of both (Li *et al.,* 2003). Thus, the zone

having high conductivity values at these depths (below 10 km) were associated with the partially melted zones in the crust. High conductivity zones in the crust of the western Anatolia are mostly explained by partially melting (Gürer, 1996; Bayrak and Nalbant, 2001; Çağlar, 2001; Tank *et al.,* 2005; Ulugergerli *et al.,* 2007). Moreover, the electrical resistivity model of Ulugergerli *et al.,* (2007) in the vicinity of the central branch of NAF is significantly similar to the geoelectrical model constructed in this study. Their model also indicates a conductor sandwiched by resistors at corresponding depths.

Dolmaz *et al.,* (2005) by analyzing aeromagnetic data estimated Curie point depth of between 8.2 and 19.9 km in western Anatolia. Aydın *et al.,* (2005) suggested the Curie point depths about 15 km along the southern branch of NAF and 10-12 km for Bursa region. Hisarlı (1995) estimated for Edremit, Susurluk and Balıkesir regions range between 8 and 12 km. The heat flow studies (Tezcan, 1979; İlkışık, 1995; Aydın *et al.,* 2005; Dolmaz *et al.,* 2005) suggested that the western Anatolia has a shallow Curie point depths, high gradients and shallow heat sources. The deepest strong conductors that are interpreted as partial melting areas are supported by heat flow maps. In other words, the thin crust, which is owing to the extensional regime in western Anatolia, may have thermal conductivity anomalies due to the fact that the shallow heat sources initiate melting at shallow depths. That is, the source of crustal conductors may be due to thermal conduction in the crust. These conductive zones may also be explained by hot springs at the region because of this the study area is close to several geothermal areas such as Gönen.

The porosity and permeability are the parameters most correlated with electrical resistivity. The resistivity decrease might be caused by the porosity and permeability increase in a medium, and vice versa. To some extent, the sharp resistivity variations in the geoelectrical models can be associated with porosity and permeability of rocks. The conductive features in the geoelectric models may be associated with the increased conductivity of pore fluids since the resistivity of crustal rocks is controlled by the resistivity of pore fluids (Archie, 1942). This might be possible if pores are interconnected with each other (Phillips *et al.,* 1995). The resistive features in the geoelectrical models may be also explained by the decreased porosity and permeability. It is assumed that the

crustal fluid resistivity as 0.04 (Nesbitt, 1993) and compaction exponent as 2, then these values yield the porosity of ~10 per cent for deep conductors (C1 and C2) and ~0.2 per cent for deep resistors (R1 and R2) from Archie' s Law (Equation 2.1). Therefore, the trapped fluids below the impermeable layers at the depth of about 13-16 km may be the reason for the conductive zones (C1 and C2) in the crust.

8. CONCLUSION

The wide band MT data were collected at 16 locations along two parallel profiles in the study area. By analyzing the data, the geoelectric strike of N102°E and N72°E were calculated for the PW and PE profiles, respectively. These values of geoelectric strikes are consistent with the NE-SW trending structural features of the regional geology (Okay *et al.,* 1991; Yılmaz *et al.,* 2010). The final electrical resistivity models aligned along these strike directions also agree well with the regional tectonic and geologic state. The MT method is based on the contrast in electrical resistivity properties of materials so as to reveal the subsurface structure. In this study, the electrical resistivity contrasts are imaged beneath two parallel profiles, with the southern highly and northern relatively resistive zones in the crust. The faults crossed by MT profiles are located in moderately resistive transition zones. The South Marmara fault (SMF) possibly corresponds to a lateral resistivity boundary between MKB and BKU on the PW and UB and MU on the PE profile. The shallow conductors along SMF are explained as fracture zones. While the crust of the south Marmara region at shallow depths is relatively conductive, it has highly resistive zones except the conductors, labeled C1 and C2 at deeper part. Since the conductive minerals cannot explain these zones, the possible reason for the conductive crust in the region is partially melting owing to the shallow Curie point depth and high heat flow values. The trapped fluids below the impermeable layers at corresponding depth (>13 km) can be another reason for the conductive zones in the crust. It would be useful to obtain the long period MT data in order to image how far the conductive zones extend and what is the geometry of them. Moreover, extending the MT profiles to further south and obtaining the ideal station spacing to investigate 3D resistivity structure of the region would give the detailed electrical resistivity structure of the south Marmara region.

APPENDIX A: OBSERVED DATA AND CALCULATED RESPONSES FROM TE AND TM MODE INVERSIONS

The following pages denote the response of apparent resistivity and phase from TE and TM mode data of the PW and PE profiles, respectively. TE and TM mode model responses are indicated with solid lines whereas observed data is demonstrated with plusses.

a)

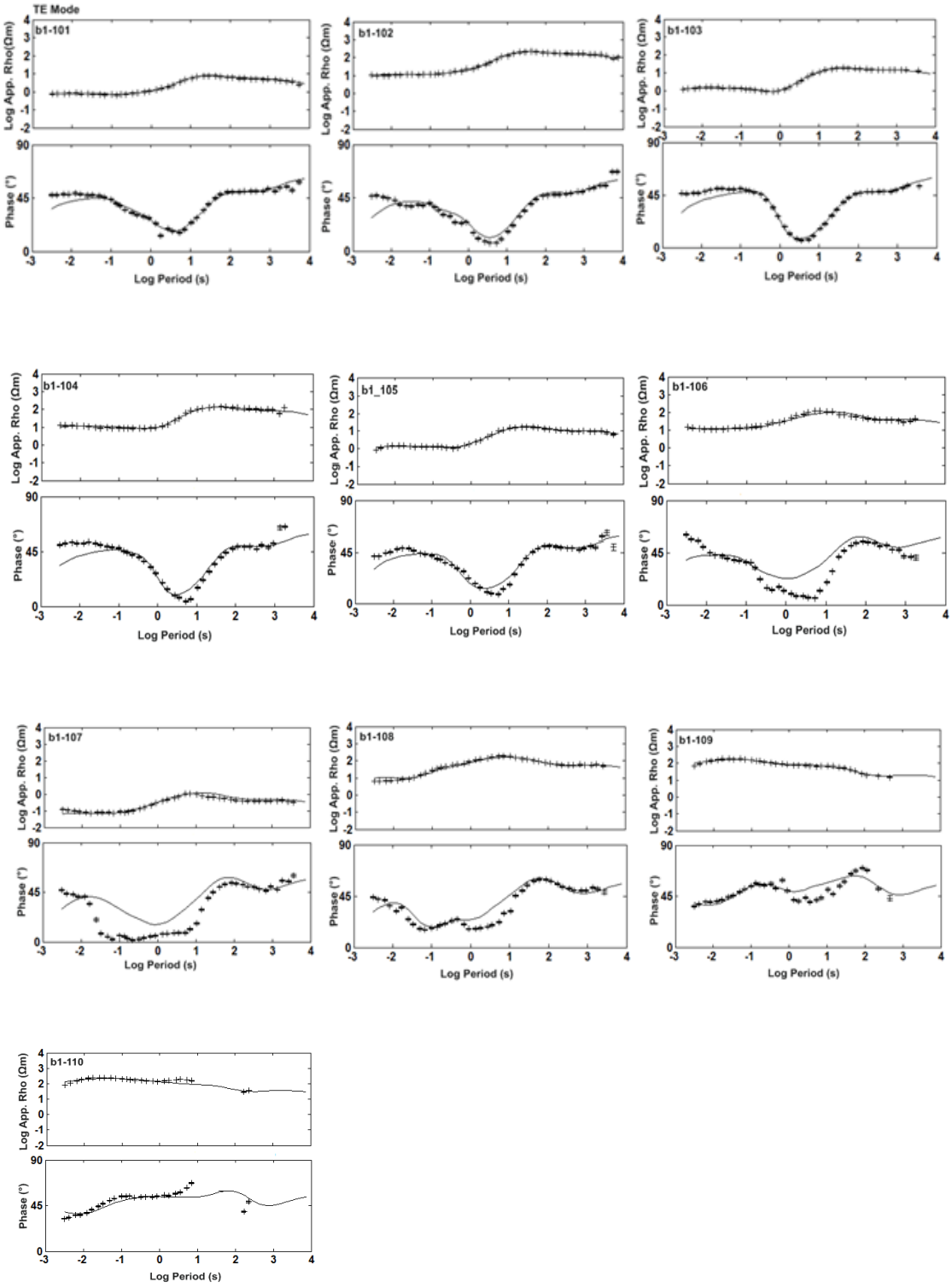
TE Mode
b1-101
b1-102
b1-103
b1-104
b1_105
b1-106
b1-107
b1-108
b1-109
b1-110
Log App. Rho (Ωm)
Phase (°)
Log Period (s)

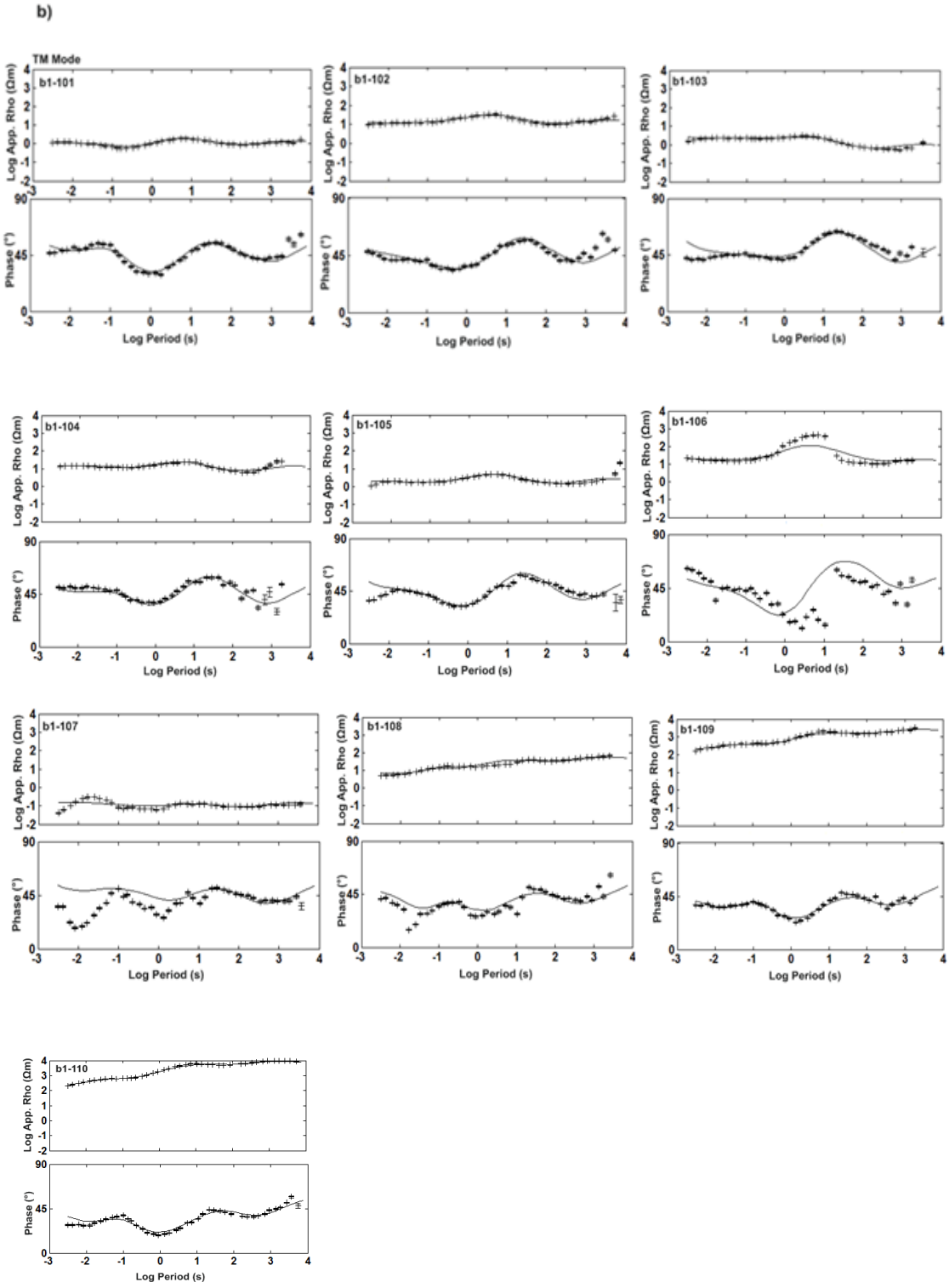

Figure A. 1. Fitting curves of observed and calculated data obtained from TM (a) and TE (b) modes of the PW profile. Solid lines represent the model response whereas plusses with error bars demonstrate the observed data

a)

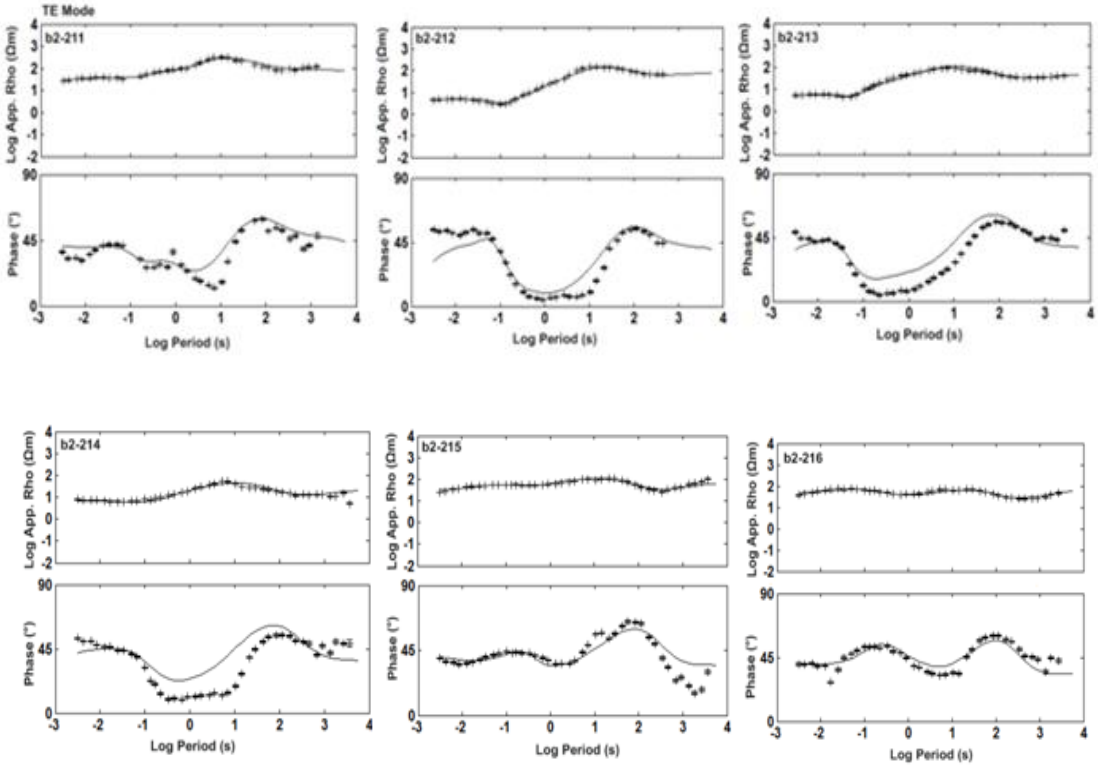
TE Mode
b2-211
b2-212
b2-213
b2-214
b2-215
b2-216
Log App. Rho (Ωm)
Phase (°)
Log Period (s)

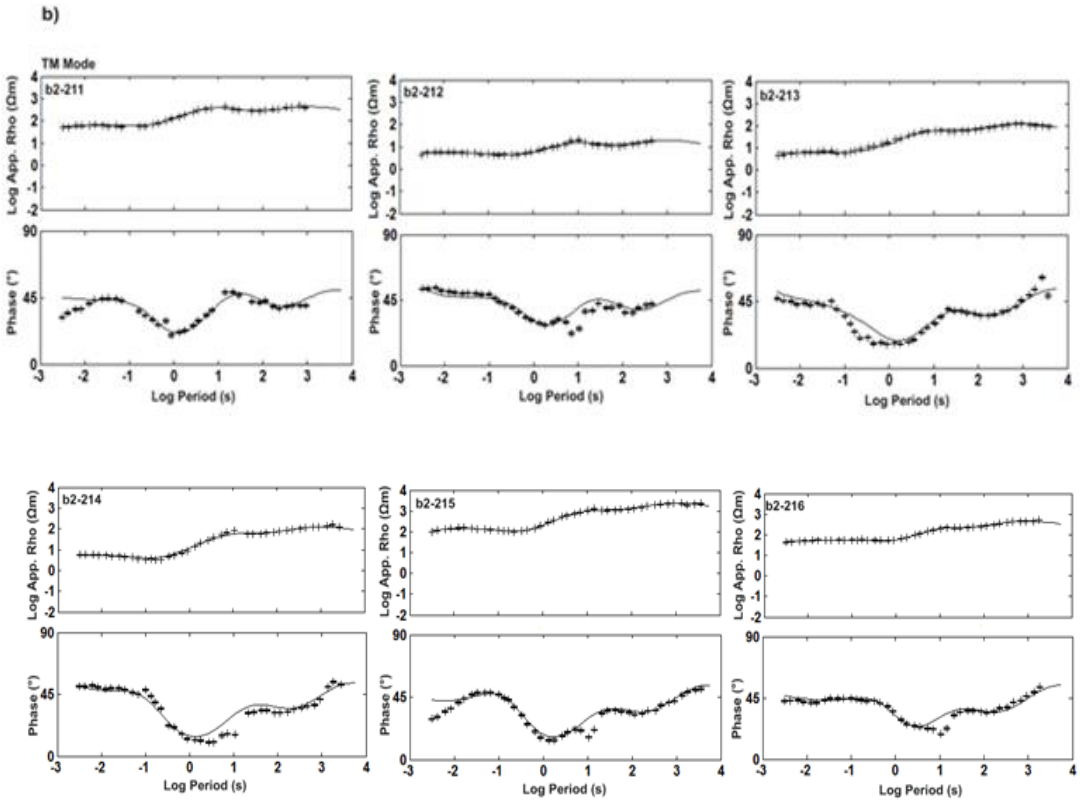

Figure A.2. Fitting curves of observed and calculated data obtained from TE (a) and TM (b) modes of the PE profile. Solid lines represent the model response whereas plusses with error bars demonstrate the observed data

REFERENCES

Adatepe, F., S. Demirel, and B. Alpar, 2002, "Tectonic Setting of the Southern Marmara Sea Region: Based on Seismic Reflection Data and Gravity Modelling", *Elsevier*, Vol. 190, pp. 383-395.

Aizawa, K., R. Yoshimura, N. Oshiman, K. Yamazaki, T. Uto, Y. Ogawa., S.B. Tank, W. Kanda., S. Sakanaka, Y. Furukawa, T. Hashimoto, M. Uyeshima, T. Ogawa, I. Shiozaki, and T. Hurst, 2005, "Hydrothermal System beneath Mt. Fuji Volcano Inferred from Magnetotellurics and Electric Self-Potential", *Earth Planet. Sci. Lett.*, Vol. 235, pp. 343-355.

Archie, G.E., 1942, "The Electrical Resistivity Log as an Aid in Determining Some Reservoir Characteristic", *Trans. Am. Inst. Min. Metall. Petr.*, Vol. 146, pp. 54-62.

Ateş, A., T. Kayiran, and I. Şençer, 2003, "Structural Interpretation of the Marmara Region NW Turkey, from Aeromagnetic, Seismic and Gravity Data", *Tectonophysics*, Vol. 367, pp. 41-99.

Ateş, A., F**.** Bilim, A. Büyüksaraç, and Ö. Bektaş, 2008, "A Tectonic Interpretation of the Marmara Sea, NW Turkey from Geophysical Data", *Earth Planets and Space.*, Vol. 60, pp. 169-177.

Aydın, I., Karat, H.I. and Koçak, A., 2005, "Curie-Point Depth Map of Turkey", *Geophys. J. Int.*, Vol. 162, pp. 633–640.

Bahr, K., 1988, "Interpretation of the Magnetotelluric Impedance Tensor: Regional Induction and Local Telluric Distortion", *J. Geophys.*, Vol. 62, pp. 119–127.

Barka, A., 1992, "The North Anatolian Fault Zone", *Annales Tectonicae*, Vol. 6, pp. 164-195.

Bayrak, M. and S.S. Nalbant, 2001, "Conductive Crust Imaged in Western Turkey by MT", *Geophys. Res. Lett.*, Vol. 28, pp. 3521–3524.

Bedrosian, P., 2007, "MT + Integrating Magnetotellurics to Determine Earth Structure, Composition and Processes", *Surveys in Geophysics*, Vol. 28, pp. 121-167.

Berdichevsky, M.N., V.I. Dmitriev, and E.E. Pozdnjakova, 1998, "On Two–Dimensional Interpretation of Magnetotelluric Soundings", *Geophys. J. Int.*, Vol. 133, pp. 585-606.

Cagniard, L., 1953, "Basic Theory of the Magnetotelluric Method in Geophysical Prospecting", *Geophysics*, Vol. 18, pp. 605-635.

Constable, S. C., A.S. Orangez, G.M. Hoversten, and H.F. Morrison, 1998, "Marine Magnetotellurics for Petroleum Exploration", *Geophysics*, Vol. 63, pp. 816-825.

Çağlar, I., 2001, "Electrical Resistivity Structure of the Northwestern Anatolia and its Tectonic Implications for the Sakarya and Bornova Zones", *Phys. Earth Planet. Inter.*, Vol. 125, pp. 95-110.

Dolmaz, M.N., Z.M. Hisarlı, T. Ustaömer, and N. Orbay, 2005, "Curie Point Depths Based on Spectrum Analysis of Aeromagnetic Data, West Anatolian Extensional Province, Turkey", *Pure Appl. Geophysics*, Vol. 162, pp. 571–590.

Erkan, K., 2008, *A Comparative Overview of Geophysical Methods*, Geodetic Science and Surveying, Columbus, Ohio.

Flerit, F., R. Armijo, G. C. P. King, B. Meyer, and A. Barka, 2003, "Slip Partitioning in the Sea of Marmara Pull-Apart Determined from GPS Velocity Vectors", *Geophys. J. Int*, Vol. 154, pp. 1-7.

Gamble, T.D., W.M., Goubau, and J., Clark, 1979, "Magnetotelluric with a Remote Magnetic Reference", *Geophysics*, Vol. 44, pp. 53-68.

Gürbüz, C., M. Aktar, H. Eyidoğan, A. Cisternas, H. Haessler, A. Barka, M. Ergin, N. Türkelli, O. Polat, S.B. Üçer, S. Kuleli, Ş. Barış, B. Kaypak, T. Bekler, E. Zor, F. Biçmen, and A. Yoruk, 2000, "The Seismotectonics of the Marmara Region (Turkey): Results from a Microseismic Experiment", *Tectonophysics*, Vol. 316, pp. 1–17.

Gürer, A., 1996, "Deep Conductivity Structure of the North Anatolian Fault Zone and İstanbul and Sakarya Zone Along Geyve-Akçakoca Profile, Northwest Anatolia", *Int. Geology Rev.*, Vol. 38, pp. 727-736.

Gürer, O.F., N. Kaymakçı, S. Çakır, M. Özburan, 2003, "Neotectonics of the Southerneast Marmara Region, NW Anatolia, Turkey", *Journal of Asian Earth Sci.,* Vol. 21, pp. 1041-1051.

Gürer, A., and M. Bayrak, 2007, "Relation between Electrical Resistivity and Earthquake Generation in the Crust of West Anatolia, Turkey", *Tectonophysics*, Vol. 445, pp. 49-65**.**

Groom, R.W., and, R.C. Bailey, 1989, "Decomposition of Magnetotelluric Impedance Tensor in the Presence of Local Three-Dimensional Galvanic Distortion", *J. Geophys. Res*., Vol. 94, pp. 1913-1925.

Haak V., and V.R.S. Hutton, 1986, "Electrical Resistivity in Continental Lower Crust", *The nature of the Lower Continental Crust*, Vol. 24, pp. 35-49.

Hisarlı, M., 1995, "Determination of the Curie Point Depths in Edremit-Susurluk Region (Turkey), *Jeofizik*, 9,10, pp. 111–117 (in Turkish).

İlkışık, O.M., 1995, "Regional Heat Flow in Western Anatolia Using Silica Temperatures Estimates from Thermal Springs", *Tectonophysics*, Vol. 244, pp. 175-184.

Jiracek, J., 1990, "Near Surface and Topographic Distortions in Electromagnetic Induction", *Surv. Geophys.*, Vol. 11, pp. 163-203.

Jiracek, G.R., V. Haak, K.H. Olsen, 1995, "Practical Magnetotelluric in a Continental Rift Environment", *Elsevier*, pp. 103-129.

Jones, A.G., 1986, "Parkinson's Pointers Potential Perfidy!", *Geophysical Journal of the Royal Astronomical Society*, Vol. 87, pp. 1215-1224.

Jones, A. G., 1999, "Imaging the Continental Upper Mantle Using Electromagnetic Methods", *Lithos*, Vol. 48, pp. 57–80.

Jödicke, H., 1992, "Water and Graphite in the Earth's Crust - an Approach to Interpretation of Conductivity Models", *Surveys in Geophysics*, Vol. 13, pp. 381-407.

Karabulut, H., S. Özalaybey, T. Taymaz, M. Aktar, O. Selvi, and A. Kocaoğlu, 2003, "A Tomographic Image of the Shallow Crustal Structure in the Eastern Marmara", *Geophysical Research Letters*, Vol. 30, pp. 10-1/10-4.

Kaufman A. A. and G.V. Keller, 1981, *The magnetotelluric sounding method, methods in geochemistry and geophysics*, Elsevier scientific publishing company.

Key, K., and S. Constable, 2002, "Broadband Marine MT Exploration of the East Pacific Rise at 9° 50' N", *Geophys. Res. Lett.*, Vol. 29, pp. 11-1/11-4.

Ledo, J., 2005, "2-D versus 3-D Magnetotelluric Data Interpretation", *Surveys in Geophys.*, Vol. 26, pp. 511-548.

Le Pichon, X., N. Chamot-Rooke, C. Rangin, and A.M.C Şengör, 2003, "The North Anatolian Fault in the Sea of Marmara", *Journal Geophysical Research*, Vol. 108, pp. 1-20.

Li, S., M.J. Unsworth, J.R. Booker, W. Wei, H. Tan, and A.G. Jones, 2003, "Partial Melt or Aqueous Fluid in the Mid-Crust of Southern Tibet? Constraints from INDEPTH Magnetotelluric Data", *Geophys. J. Int.*, Vol. 153, pp. 289-304.

Lilley (Ted), F.E.M., 1998, "Magnetotelluric Tensor Decomposition: Part II, Examples of Basic Procedure", *Geophysics*, Vol. 63, pp. 1898-1907.

McNeice, G.W., and A.G., Jones, 2001, "Multisite, Multifrequency Tensor Decomposition of Magnetotelluric Data", *Geophysics*, Vol. 66, pp. 158-173.

Meade, B. J., B. H. Hager, S.C. McClusky, R. Reilinger, S. Ergintav, O. Lenk, A. Barka and H Ozener, 2002, "Estimates of Seismic Potential in the Marmara Sea Region from Block Models of Secular Deformation Constrained by Global Positioning System Measurements'', *Bull Seismol. Soc. Am.*, Vol. 92, pp. 208-215.

Nesbitt, B. E., 1993, "Electrical Resistivities of Crustal Fluids", *J. Geophys. Res.*, Vol. 98, pp. 4301-4310.

Nowack, R. L., 2002, *EAS657- Geophysical Inverse Theory Lecture Notes, Lecture1*, http://web.ics.purdue.edu/~nowack/eas657.html

Nurhasan, Y. Ogawa, N. Ujihara, S.B. Tank, Y. Honkura, S. Onizawa, T. Mori, and M. Makino, 2006, "Two Electrical Conductors beneath Kusatsu-Shirane Volcano, Japan, Imaged by Audiomagnetotellurics, and their Implications for the Hydrothermal System", *Earth Planets Space*, Vol. 58, pp. 1053-1059.

Nyst, M. and W. Thatcher, 2004, "New Constraints on the Active Tectonic Deformation of the Aegean", *Journal of Geop. Research*, Vol. 109, B11406-B11, pp. 1-23.

Okay, A.I., M. Siyako, and K.A. Bürkan, 1991, "Geology and Tectonic Evolution of the Biga Peninsula, Northwest Turkey", *Bull. of the Technical University of İstanbul*, Vol. 44, pp. 191-255.

Ogawa, Y., and T. Uchida, 1996, "A Two-Dimensional Magnetotelluric Inversion Assuming Gaussian Static Shift", *Geophys. J. Int.,* Vol. 126, pp. 69-76.

Ogawa, Y., 2002, "On Two Dimensional Modeling of Magnetotelluric Field Data", *Surveys in Geophysics*, Vol. 23, pp. 251-272.

Park, S.K., G.P. Biasi, R.L. Mackie and T.R. Madden, 1991, "Magnetotelluric Evidence for Crustal Suture Zones Bounding the Southern Great Valley, California", *Journal of Geophysical Research*, Vol. 96, pp. 353-376.

Parkinson, W.D., 1962, "The Influence of Continents and Oceans on Geomagnetic Variations", *The Geophysical Journal of the Royal Astronomical Society,* Vol. 6, pp. 411-449.

Phillips, D.E., W.D. Stanley, B.D. Rodriguez, and, W.J. Lutter, 1995, "Surface Seismic and Electrical Methods to Detect Fluids Related to Faulting", *Journal of Geophysical Research*, Vol. 12, pp. 919-936.

Reynolds, J.M., 1997, *An Introduction to Applied and Environmental Geophysics*, John Wiley and Sons, Inc., Newyork.

Ritter, O., A. Hoffmann-Rothe, P. A. Bedrosian, U. Weckmann and V. Haak, 2005, "Electrical Conductivity Images of Active and Fossil Fault Zones", *The Geological Society of Londan, special Publications*, Vol. 245, pp. 165-186.

Selim, H.H., 2004, *Kuzey Anadolu Fayı'nın Güney Koluna ait Yenice-Gönen, Manyas-Mustafakemalpaşa, Uluabat ve Bursa Faylarının Morfolojik, Sismolojik ve Jeolojik Özellikleri*, Avrasya Yer Bilimleri Enstitüsü, Doktora Tezi, İTÜ.

Selim, H.H., and O. Tüysüz, 2005, " Evolution of Pull-Apart Basins in the South Marmara Region, NW Turkey", *Geophysical Research Abstracts*, Vol. 7.

Selim, H.H., O. Tüysüz, and A.A. Barka, 2006, "Güney Marmara Bölümü' nün Neotektoniği", *İTÜ Dergisi*, Vol. 5, pp. 151-160.

Simpson, F. and K. Bahr, 2005, *Practical Magnetotellurics*, Cambridge University Press.

Swift C. M., 1967, *A Magnetotelluric Investigation of an Electrical Conductivity Anomaly in the South-Western United States*, Ph.D. Thesis, M.I.T.

Şengör, A.M.C., N. Görür, and F. Şaroğlu, 1985, "Strike-Slip Deformation Basin Formation and Sedimentation: Strike-Slip Faulting and Related Basin Formation in Zones of Tectonic Escape: Turkey as a Case Study. In: Biddle, K.T. and Christie-Blick, N. (Eds.), Strike-Slip Faulting and Basin Formation", *Society of Economic Paleontologists and Mineralogist, Special Publication,* Vol. 37, pp. 227-264.

Tank, S. B., Y. Honkura, Y. Ogawa, M. Matsushima, N. Oshiman, M. K. Tunçer, C. Çelik, E. Tolak, and A. M. Işıkara, 2005, "Magnetotelluric Imaging of the Fault Rupture Area of the 1999 İzmit (Turkey) Earthquake", *Phys. Earth Planet. Inter*., Vol. 150, pp. 213–225.

Taymaz, T., O. Tan, and S. Yolsal, 2004, "Active Tectonics of Turkey and Surroundings and Sesmic Risk in the Marmara Sea Region*"*, S2-03, *The Proceedings of IWAM04*, Mizunami, Japan.

Tezcan, A.K., 1979, "Geothermal Studies, their Present Status and Contribution to Heat Flow Contouring in Turkey, in Terrestrial Heat Flow in Europe", eds Cermak, V. & Rybach, L., Springer Verlag, Berlin, pp. 283–291.

Tikhonov, A.N., 1950, "On Determining Electrical Characteristics of the Deep Layers of the Earth's Crust", *Doklady*, Vol. 73, pp. 281-285.

Tuncer, V., M.J. Unsworth, W. Siripunvaraporn, and J.A. Craven, 2006, "Exploration for Unconformity-Type Uranium Deposits with Audiomagnetotellurics Data: A Case

Study from the McArthur River Mine, Saskatchewan, Canada", *Geophysics,* Vol. 71, pp. 201-209.

Uchida, T., 1993, "Smooth 2-D Inversion of Magnetotelluric Data Based on Statistical Criterion ABIC", *J. Geomag. Geoelectr.*, Vol. 45, pp. 841-858.

Ulugergerli, E.U., G. Seyitoğlu, A.T. Başokur, C. Kaya, U. Dikmen, and M.E. Candansayar, 2007, " The Geoelectrical Structure of Northwestern Anatoli, Turkey*", Pure Appl. Geophys,* Vol. 164, pp. 999-1026.

Unsworth, M., 2010, *Geoph424 Lecture Notes*, http://www.ualberta.ca/~unsworth/UA-classes/424/notes424-2010.html .

Vozoff, K., 1972, "The Magnetotelluric Method in the Expolaration of Sedimentery Basins", *Geophysics*, Vol. 37, pp. 98-141.

Vozoff, K., 1991, "The Magnetotelluric Method", in Nabighian, M. N., Ed., Electromagnetic Methods in Applied Geophysics: SEG., *2B*, 641-711.

Ward, Stanley H., and G. W., Hohmann, 1988, "Electromagnetic Theory for Geophysical Applications", *Electromagnetic Methods in Applied Geophysics*, Vol. 1, pp. 130-311.

Yılmaz, H., S. Över, and S. Özden, 2006, Kinematics of the East Anatolian Fault Zone between Turkoğlu (Kahramanmaraş) and Çelikhan (Adıyaman), Eastern Turkey", *Earth Planets Space*, Vol. 58, pp. 1463–1473.

Yılmaz, Y., E. Gökaşan, and A.Y. Erbay, 2010, "Morphotectonic Development of the Marmara Region", *Tectonophysics*, Vol. 488, pp. 51-70.

Zhao, D., H. Kanamori, and H. Negishi, 1996, "Tomography of the Source Area of the 1995 Kobe Earthquake: Evidence for Fluids at the Hypocenter?", *Science*, Vol. 274, pp. 1891–1894.